



Representing extreme fires and their radiative effects in a global climate model via variable scaling of emissions: Case study of the 2020 California wildfires

Elizabeth Quaye¹, Ben T. Johnson², James M. Haywood¹, Guido R. van der Werf³, Roland Vernooij³,
Stephen A. Sitch⁴ and Tom Eames^{1,4}

¹Department of Mathematics and Statistics, University of Exeter, Exeter, UK

²Met Office Hadley Centre, Exeter, UK

³Meteorology and Air Quality Group, Wageningen University & Research, Wageningen, Netherlands.

⁴Department of Geography, University of Exeter, Exeter, UK

Correspondence to: Elizabeth Quaye (ehq201@exeter.ac.uk), Ben T. Johnson (ben.johnson@metoffice.gov.uk)

Abstract. An accurate representation of biomass burning aerosol emissions is essential in Earth System Models to capture aerosol properties and reduce uncertainties in their interactions with radiation and climate. Sources of wildfire smoke include both widespread prevalence of numerous small fires and more extreme episodic events, such as the unprecedented Californian wildfires of September 2020. Our global modelling study leverages observational data to evaluate how well aerosol emissions from extreme wildfires are captured in the UK Earth System Model (UKESM), alongside those from other fires. Running with daily emissions from Global Fire Emission Database v.4.1s (GFED4.1s) enables a realistic simulation of the thick smoke plumes from the Californian fires and large boreal fires more generally, with little overall bias in aerosol optical depths (AODs) between UKESM and co-located observations (AERONET, VIIRS). However, modelled AODs were biased low across other regions (e.g. savannah) dominated by fires with lower fuel consumption, unless emissions were scaled up by a factor of 2. We therefore develop a means of selectively scaling up aerosol emissions from GFED4.1s pixels with lower area-averaged daily dry matter consumption (DM) and not scaling those with higher daily DM, associated with extremely large or intense fires. Applying daily emissions was crucial in capturing the spatial and temporal variability of AOD and instantaneous radiative forcing (IRF) during extreme events, although switching to monthly emissions made little difference to the regional monthly mean IRF. Our results indicate a way forward to ensure both means and extremes in biomass burning smoke events are represented.

1 Introduction

1.1 Biomass burning aerosol and their radiative impacts

Biomass burning aerosols (BBA), consist mostly of organic carbon (OC) and black carbon (BC) with nitrate and sulphate aerosols found in smaller quantities (Haywood et al., 2021) and can significantly impact the climate due to their interactions with radiation and clouds. Scattering of solar radiation has a negative radiative effect (i.e. a cooling impact) and is dominated by non-absorbing or weakly absorbing aerosol components including sulphates, nitrates, ammonium, organic carbon and



sea-salt particles (Boucher, 2015; Li et al., 2022). Absorption of solar radiation by black carbon, and to a lesser extent by brown carbon (i.e. the absorbing component of organic carbon) (e.g. Forrister et al., 2015), exerts a positive radiative effect (i.e. a warming impact). The single scattering albedo of BBA is close to the balance point, where reflection and absorption of sunlight have similar but opposing effects on radiation balance at the top of the atmosphere (TOA) (Haywood and Shine, 1995), leading to an estimated direct radiative forcing of $\pm 0.2 \text{ Wm}^{-2}$ (Boucher et al., 2014). Where BBA exists above open ocean, it will typically increase planetary albedo, thus exerting a negative radiative effect. Above bright stratocumulus, it can decrease the planetary albedo, exerting a positive radiative effect (e.g. Peers et al., 2021). Therefore, the climate impact of fire events directly depends on its location and that of the downwind plume (i.e. plume height and whether over land or ocean), and the meteorological conditions (cloud vs cloud free), and thus temporal resolution of assessments is likely important consideration in overall climate impacts of extreme fire events. Absorption of solar radiation by aerosols also exerts a strong feedback on clouds and atmospheric circulation (e.g. Johnson et al., 2019).

The radiative effects of BBA can also impact on local meteorology. For example, in September 1987, aerosols emitted from Californian fires were trapped by a temperature inversion in a valley for three weeks, causing the local daily maximum temperature to decrease by an average 15°C in the week after the fire, and by 5°C for the following three weeks, due to radiative effects (Robock, 1988). Conversely, it has been noted that recently burned areas may have a lower surface albedo (appearing blackened) raising the possibility of localised surface warming (Yin and Roy 2005; Randerson et al., 2006).

Quantifying aerosol radiative effects of wildfire events is critical, particularly as fire activity and emissions change over time (e.g. Zheng et al. 2021) and more frequent extreme fire events have been linked to climate change (Ellis et al., 2022; Jones et al., 2022; Jones et al., 2024). A study by Dennison et al. (2014) found that in the western United States, between 1984 and 2011, the fire-affected area increased on average by 355 km^2 per year, with the analysis of trends indicating at least a doubling of the number of large fires ($> 405 \text{ ha}$) identified during that period. This comes with a proportional increase in emissions and hence AOD, with the uncertainty in radiative forcing increasing correspondingly. Thus, it is essential that BBA is accurately represented in global climate and Earth System models.

1.2 Implementing biomass burning aerosol emissions in global models

Biomass burning emissions of organic and black carbon from satellite-based products such as the Global Fire Emission Database (GFED) are widely used as inputs by climate and Earth System models to include this important aerosol source in climate simulations of the recent past (Thornhill et al., 2018; Shinozuka et al., 2020; Johnson et al., 2016). Such simulations often employ monthly rather than daily means and routinely apply a global scaling factor ranging between 1.02 to 6 depending on the model, aerosol scheme, and biomass burning emission inventory (Marlier et al., 2013; Matichuk et al., 2008; Reddington et al., 2016; and more recently, Petrenko et al., 2024). Regional scaling factors have also been applied, as in Johnston et al. (2012) and Ward et al. (2012), which applied different scaling factors for 14 continental-scale regions. Alternatively, Sakaeda et al. (2011) applied a scaling factor of 2 to organic and black carbon masses between $10\text{--}30^\circ\text{N}$ and $-20\text{--}50^\circ\text{E}$. Such scaling has been justified in part as a pragmatic necessity to improve agreement between modelled and



65 observed aerosol concentrations and AODs. One well documented source of this discrepancy is the difficulty of detecting
smaller fires from space that still contribute substantially to emissions (e.g. Ramo et al., 2021). For instance, a recent study
by van der Velde et al. (2024) used higher resolution satellite imagery (20 m) to better identify burn scars than previous
burned area products. Incorporating the previously unresolved small fires led to increases of up to 120 % in estimated
emissions of carbon monoxide and lower biases between modelled and satellite retrievals of atmospheric carbon monoxide
70 concentrations. It is also possible that variations in emission factors (EFs) across the season may influence the degree to
which different species are emitted. Emission factors can vary with seasonality and/or dominant weather conditions at the
time of a fire (Vernooij et al., 2023). As shown in Li et al. (2025), other emissions inventories such as those based on active
fire / thermal anomalies can also suffer from the same scaling issues as GFED. The study used a ‘top-down’ approach to
scale NOAA’s GBBEPx v3 fire emissions data (derived from fire radiative power detections) based on their modelled versus
75 observed AODs. They found that emissions were underestimated for smaller fires and overestimated for larger fires.
For simulations with the Hadley Centre Global Environment Model (HadGEM3-GA7) using GLOMAP-mode as the aerosol
scheme, Johnson et al. (2016) found a scaling factor of 2 on GFED emissions gave the best fit between modelled and
observed AOD over tropical biomass burning regions. The magnitude of the modelled AOD and thus the required scaling
factor was shown to depend on the model’s assumptions for water uptake by the BBA and oxidation and condensation
80 processes (Johnson et al., 2016), but was more generally considered necessary to represent the emissions from small fires
which may be sub-pixel and/or underlying large vegetative canopies and thus are undetected by burnt area satellite retrievals
(Randerson et al., 2012; United Nations Environment Programme, 2022). Whilst corrections were applied in the
development of GFED4.1s, these were later shown to be too conservative (Chen et al., 2023; Ramo et al., 2021). The same
scaling factor has been applied to BBA emissions in subsequent coupled configurations of HadGEM3 and UKESM1
85 (Mulcahy et al., 2020). A recent study of CH₄ emissions from wildfires found a 27 % underestimation in widely used fire
emission models compared to satellite approximations, attributing this to undetected small fires (Zhao et al., 2025).

1.3 The contribution of extreme fires to biomass burning aerosol emissions

Extreme fire events, or ‘megafires’, defined as ‘fires that burn over 10 thousand hectares arising from single or multiple
related ignition events’ (Linley et al., 2022), have become more prevalent in recent years due to land use change and climate
90 change resulting in hotter, drier weather, stronger winds, and new fuel availability (United Nations Environment Programme,
2022; Duane et al., 2021). The year 2020 was an exceptional year for extreme fire events, with the Australian Black Summer
fires occurring at the late end of 2019 and early 2020, the northeast Siberian fires taking place throughout June to October.
This study focuses mostly on the Californian fires in August and September 2020 (Nolan et al., 2022). Daily emissions of
BC and OC for the aforementioned extreme fire events are shown in Fig. 1, where black represents the total global
95 emissions. Regions of extreme fire occurrence in 2020 are shown in red (southeast Australia), orange (northeast Siberia), and
blue (western US). Emissions from these regions during extreme fire events dominate the peaks in the timeseries of global
daily emissions, indicating they dominate those from the rest of the world at such times, even throughout the African



(December to March in the north, June to November in the south) and South American (August to November) burning seasons. The highest emission day was on the 9th of September, with 0.29 Tg of OC and BC, 0.19 Tg of this coming from the western US (region bounded by -125–115° E, 30–50° N).

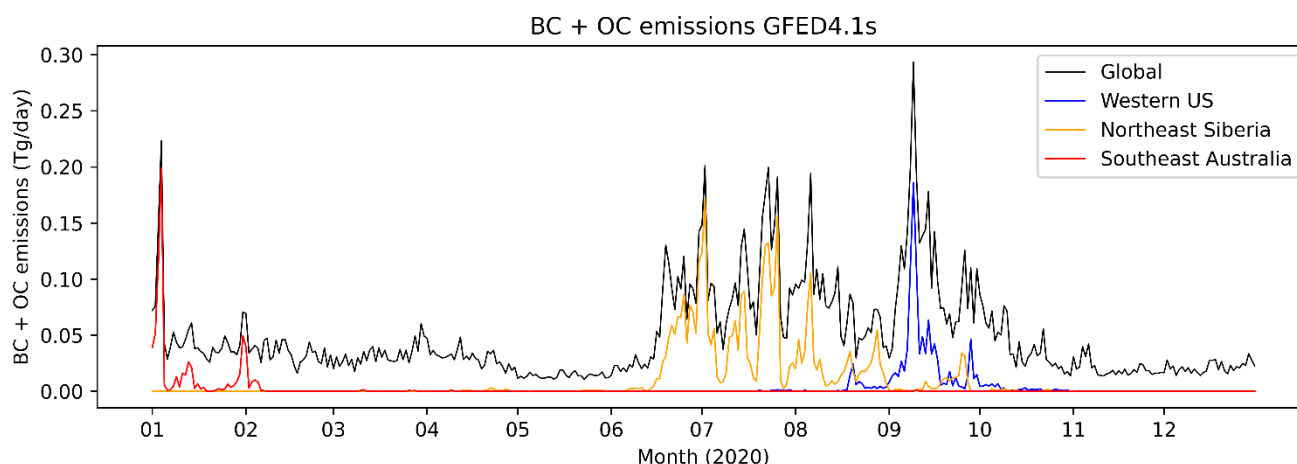


Figure 1: Combined organic carbon (OC) and black carbon (BC) emissions over the year 2020 from GFED4.1s. Black line shows the global total. Blue line shows the western United States emissions (-125–115° E, 30–50° N). Orange line shows the northeast Siberian emissions (90–175° E, 55–80° N). Red line shows southeast Australian emissions (140–180° E, -30–45° N).

The 2020 Western US fires were the largest recorded in the California’s modern history (<https://www.fire.ca.gov/incidents/2020/>; Ceamanos et al., 2023), burning an area of over 4.3 million acres (Smith, 2020), with the month of greatest fire activity being September. In this time, around 1.16 Tg of BC and OC was injected into the atmosphere according to GFED4.1s estimates. MODIS Corrected Reflectance over North America is shown in Fig. 2 for the 8th, 10th, 12th and 14th September 2020. Optically thick smoke can be identified by its yellow/grey colour, which differentiates it from bright white clouds. The image illustrates how the smoke perturbation caused either a positive or negative radiative forcing, depending on the underlying fraction of stratocumulus cloud, and surface reflectance. This aerosol mass initially advected over the Pacific Ocean (Fig. 2a, 2b, 2c), before drifting eastward across North America and the Atlantic (Fig. 2c, 2d), ultimately taking only 3–4 days to travel from US west coast to Europe (Baars et al., 2021).

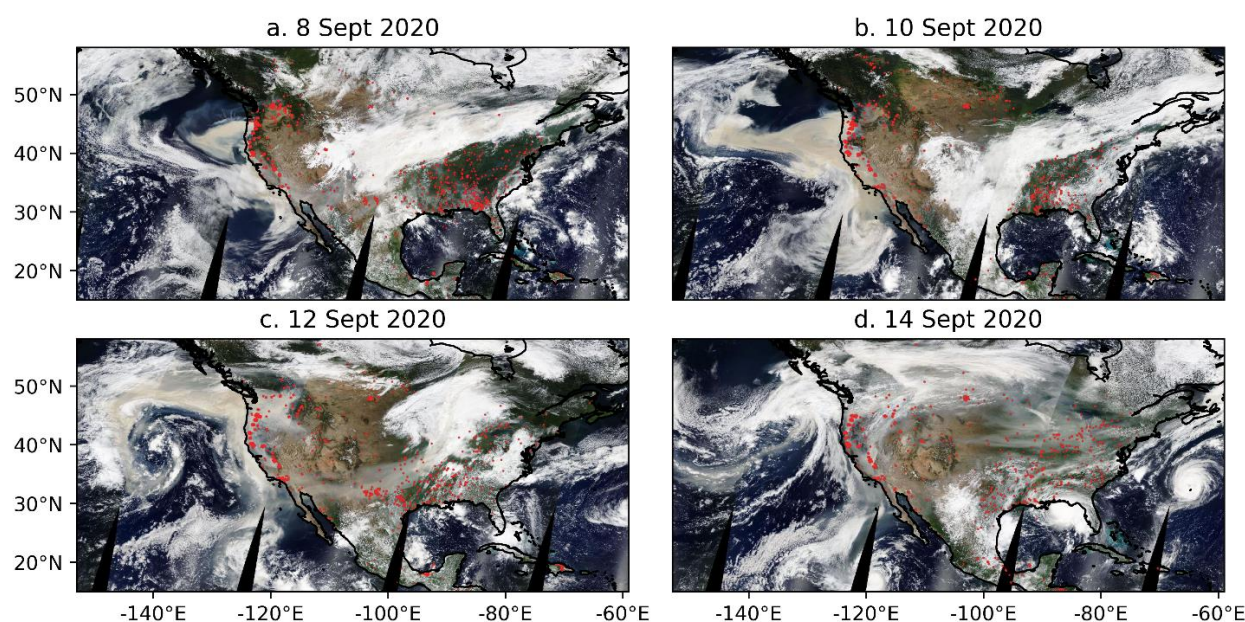


Figure 2: MODIS Corrected Reflectance imagery over North America for 8th, 10th, 12th, and 14th September 2020. Red shows active fire detections and thermal anomalies from Suomi NPP / VIIRS (Visible Infrared Imaging Radiometer Suite) Fire and Thermal Anomalies (Day and Night, 375 m). Imagery from the Worldview Snapshots application (<https://wvs.earthdata.nasa.gov>), part of the Earth Science Data and Information System (ESDIS)

1.4 Objectives

In this study we evaluate how well extreme fires can be represented in a global climate model which typically uses monthly mean emissions data as its source term and aims to simulate climate on monthly to centennial timescales. Specifically, we investigate firstly the use of global emission scaling factors and, secondly the use of monthly mean rather than higher temporal resolution data (e.g. daily).

Globally uniform scaling factors could cause an overestimation of BBA for extreme fire events where the fire or burnt area is more readily identifiable from satellites, due to their size, intensity and potentially more complete burning of vegetative layers, including the canopy. Monthly emissions data may fail to capture the variability in intensity and geographic spread of BBA plumes, which, considering their radiative interactions (partial absorption and multiple scattering), could result in widely different radiative effects (De Graaf et al., 2014).

Using satellite observations, we validate the modelled geographic aerosol distribution. We determine the most appropriate emissions scaling approach in the model, using this to assess the magnitude of the instantaneous radiative forcing, comparing daily mean with monthly mean emissions simulations to examine the biases of using the ‘standard’ monthly averages. We determine the radiative effects on a regional scale and quantify the potential for individual extreme fire events to contribute to radiative forcing globally.



2 Data and Methods

2.1 UKESM1.1 Model Configuration

Global model simulations were performed with UK Earth System Model (UKESM) version 1.1, an updated configuration aimed at reducing a cold bias in UKESM1 historical simulations. The changes are described in Mulcahy et al. (2023) and include an improved parameterisation of SO₂ dry deposition, and a range of minor changes to the aerosol scheme. The description and evaluation of UKESM1 is detailed by Sellar et al. (2019). The fully coupled Earth System model uses the Joint UK Land Environment Simulator (JULES) for terrestrial biogeochemistry (Clark et al., 2011), the Model of Ecosystem Dynamics, nutrient Utilisation, Sequestration and Acidification (MEDUSA) for ocean biogeochemistry (Yool et al., 2013), the United Kingdom Chemistry and Aerosol model (UKCA) for atmospheric composition (Archibald et al., 2019), and the coupled atmosphere-ocean model HadGEM3-GC3.1 as the physical core (Kuhlbrodt et al., 2018). In this study we use the atmosphere-only configuration in which the state of the ocean and terrestrial biosphere do not evolve interactively but are taken from analyses and/or prior simulations with the fully coupled model. The model has a resolution of 1.25° latitude × 1.875° longitude, with 85 vertical levels and includes a two-moment pseudo-modal aerosol microphysics scheme: the Global Model of Aerosol Processes (GLOMAP), which simulates mass and number for individual aerosol classifications (sulphate, sea salt, black carbon and organic carbon) across five lognormal size modes (Mann et al., 2010). Absorption of UV and visible radiation by organic carbon is not represented (i.e. brown carbon and its subsequent bleaching is neglected). Furthermore, whilst GLOMAP-mode does represent various ageing processes, including the condensate of sulphate onto carbonaceous aerosol, the coagulation and internal mixing with other aerosol components and the subsequent increase in solubility, our model does not account for condensation and evaporation of organics. Mineral dust is simulated separately using a six-bin emission scheme (Mulcahy et al., 2018; Woodward, 2001).

2.2 Experimental design

The simulations are set up with greenhouse gas concentrations and aerosol-chemistry emissions from the sixth Coupled Model Intercomparison project (CMIP6), taking inputs from the Shared Socioeconomic Pathways (SSP) 2-4.5 scenario to represent present-day climate (Sellar et al., 2020). The simulations included a month's spin up followed by a 2-year simulation for the period 2019 – 2020. Nudging is applied to the simulations, relaxing the horizontal winds towards ERA5 reanalyses (Hersbach et al., 2020) with a 6-hour relaxation timescale. Simulations are not nudged to temperature, allowing the thermodynamics to adjust to heating from aerosol absorption, following the same rationale and methodology as in Johnson et al. (2019).

Daily and monthly emissions of organic carbon and black carbon from biomass burning (BB) for the years 2019 and 2020 are extracted from the beta version of the Global Fire Emissions Database version 4.1s (<https://www.geo.vu.nl/~gwerf/GFED/GFED4/>; Randerson et al., 2017), which includes small fires corrections (van der Werf et al., 2017). Smoke plume rise is not explicitly modelled, but the initial vertical profile is prescribed based on the



GFED vegetation type. Fire emissions deriving from peat, savannah and woodland are emitted at the lowest vertical level, and forest and tropical fire emissions are injected uniformly between 0 and 3 km, based on simplifying the Aerosol InterComparison project (AeroCom) recommendations on injection heights for wild-land fires from different geographical locations and vegetation types (Dentener et al., 2006).

2.2.1 Global Fire Emissions Database GFED4.1s scaling factors applied to the simulations

Simulation	GFED4.1s emissions (E)
NOFIRE	None
FIRE_1X	$1 \times E$ (daily mean)
FIRE_2X	$2 \times E$ (daily mean)
FIRE_DM	$2 \times E$ for $DM < 50$, linear ramp $2 \rightarrow 1 \times E$ for $50 < DM < 200$, $1 \times E$ for $DM > 200$ (daily mean)
FIRE_DM_MO	Same as FIRE_DM but averaged into monthly means

Table 1: List of simulations in this study, each with a different emission scaling factor / method. DM = Dry Matter (fuel) consumed per GFED pixel per day in units of $gm^{-2}day^{-1}$.

The Global Fire Emissions Database (GFED) is based on the Carnegie-Ames-Stanford Approach (CASA) model of the terrestrial carbon cycle (Potter et al., 1993), which is adjusted to account for fires. The data is derived from vegetation characteristics (computed from the fraction of absorbed photosynthetically active radiation, fractional tree cover, and land cover), meteorology from the ERA-interim dataset (Dee et al., 2011), and satellite observations of burnt area from MODIS (van der Werf et al., 2017). For years 2017 – 2023, the GFED4.1s emissions are not based on burned area but instead are estimated for each 0.25° grid cell based on the ratio between MODIS active fire detections and GFED4.1s between 2003 to 2016. It is estimated that this approach gives the accuracy to within 2 % of the original data, with early season fires slightly amplified (<https://www.geo.vu.nl/~gwerf/GFED/GFED4/Readme.pdf>).

The five simulations in this study include variations of the way that GFED4.1s emissions of black carbon and organic carbon are scaled (Table 1). In simulation NOFIRE, there are no BC or OC emissions from fires. In FIRE_1X, the daily GFED4.1s emissions are unscaled in the simulation (i.e. we apply the standard GFED4 emission factors used to derive BC and OC emissions from the dry matter consumed with no additional scaling). In FIRE_2X, the daily emissions are globally multiplied by a factor of two, as is routinely applied in HadGEM3 and UKESM1, following the analysis in Johnson et al. (2016). In FIRE_DM, the daily emissions are multiplied by a scaling factor which is dependent on the daily dry matter (DM) consumption, estimated by GFED per grid-cell. The aim of this approach is to apply a scaling factor that is dependent on the



size and/or intensity of fires, since these quantities are potentially linked to both detectability of fires from space (Ramo et al., 2021; Randerson et al., 2012), and to possible (seasonal) emission factor changes (Vernooij et al., 2023). Post 2016 GFED4.1s emission were based on MODIS fire count, which rely on a detectable heat signature from active fires. Estimates of burned area were therefore not available within the GFED4.1s product during 2020 and the daily estimate of DM consumption provides the indicator of the scale of the fire (essentially the product of burned area and fuel load). Based on the analysis presented in section 3.1, pixels with daily DM lower than 50 gm⁻² DM adopt a scaling of 2, and grid cells with DM higher than 200 gm⁻² are unscaled. For grid cells with DM between 50 and 200 gm⁻², the OC and BC multiplication factor is determined by a linear ramp function, between 2 and 1. In FIRE_DM_MO, the daily emissions from FIRE_DM are averaged into monthly means.

2.3 Observational data

The AErosol RObotic NETwork (AERONET) is a network of ground-based Sun photometers that measure AOD and retrieve other properties of atmospheric aerosol, including aerosol refractive index, volume, size distribution, and single scattering albedo (Holben et al., 1998). In this investigation AOD observations from 77 north American AERONET sites are utilised. These were selected due to the availability of level 2 data across the period of the study (1–30th September 2020). This includes pre- and post-field calibration, cloud-screening and manual quality-control (Giles et al., 2019; Smirnov et al., 2000). Data from AERONET is available at wavelengths, λ , of 340, 380, 500, 675, 870, 1020 and 1640 nm. The Ångström exponent, α , was calculated for each AERONET retrieval using the AOD at 500 nm and 675 nm, which was used to estimate the AOD at 550 nm (Eq. 1) (Schuster et al., 2006).

$$\alpha = - \frac{\log\left(\frac{AOD_{\lambda_1}}{AOD_{\lambda_2}}\right)}{\log\left(\frac{\lambda_1}{\lambda_2}\right)}, \quad (1)$$

This study uses satellite AOD data from Visible Infrared Imaging Radiometer Suite (VIIRS) Deep Blue, onboard the Suomi National Polar-orbiting Partnership (Suomi NPP) satellite (Jackson et al., 2013) (https://ladsweb.modaps.eosdis.nasa.gov/missions-and-measurements/products/AERDB_D3_VIIRS_SNPP). The level 3 gridded data has a horizontal resolution of 1° x 1°. Deep Blue (DB) consists of the DB algorithm over land, and Satellite Ocean Aerosol Retrieval (SOAR) over ocean (Sawyer et al., 2020). Blue wavelengths are used due to minimal surface reflectance which improves retrievals over bright surface. Wang et al. (2023) showed that Suomi VIIRS DB had a correlation coefficient of 0.880, and root mean square error (RMSE) of 0.158 in their evaluation against AERONET. In a case study of the 2020 Californian wildfires, they showed its capability to capture extreme aerosol optical depths from biomass burning, additionally finding correlation coefficients greater than 0.85 in comparison with all nine of investigated AERONET sites.



Daily mean gridded total column density of carbon monoxide (CO) data from the Tropospheric Monitoring Instrument (TROPOMI) (Veefkind et al., 2012), onboard the European Space Agency's (ESA) Sentinel-5P satellite, is used as a constraint when comparing AOD data from model and observation. A mask excluding grid cells of CO less than 100 ppbv (parts per billion by volume) was applied to AOD data, in order to reject locations where the aerosol was less likely to have originated from biomass burning. This value was chosen due to being the average background concentration in the atmosphere (Zheng, 2019). In a study of biomass burning in the southern hemisphere, a strong correlation was found between CO column loading and AOD (Edwards et al., 2006), a caveat being that CO has a longer tropospheric lifetime than aerosol (Khalil and Rasmussen, 1990), thus, older CO contributes to the total column loading. Whilst this technique is not perfect, it eliminates much of the AOD not associated with biomass burning. Statistical analyses were also performed on unmasked AOD data, and we found that while masking AOD didn't improve the correlation, it eliminated low AODs. Of the unmasked data, 48 % of the points had low AODs of less than 0.1, causing potential bias in the results, compared to only 17 % of the masked data having AODs of less than 0.1. In global analyses, regions are selected based on the occurrence of biomass burning. The combination of these approaches eliminates significant contributions from other anthropogenic sources.

2.4 Instantaneous radiative forcing

The instantaneous radiative effect (IRE) of aerosol is calculated as the difference between the polluted (clouds + aerosols) and clean (clouds + no aerosols) TOA shortwave upwelling flux: $IRE = -(polluted - clean)$. Only shortwave radiation is considered in this study as longwave radiative effects were typically an order of magnitude lower in our simulations, whereas the shortwave effects dominated and were strongly connected to the AOD (at solar wavelengths). The instantaneous radiative forcing (IRF) is calculated as the difference between biomass burning simulations (FIRE_1X, FIRE_2X, FIRE_DM), and a control simulation with no BBA emissions (NOFIRE), run over the same time period with sea surface temperatures, sea ice, and greenhouse gas concentrations remaining fixed: e.g. $IRF_{FIRE_1X} = IRE_{FIRE_1X} - IRE_{NOFIRE}$ (Johnson et al., 2019).

2.5 Regions of analysis

We identified five regions (Table 2), including the western US, which have strong biomass burning contributions, with minimal interference from other aerosol sources such as anthropogenic emissions and dust, which is not the focus of this study. With exception of southeast Australia, where the extreme 'Australian Black Summer' wildfire event occurred at the end of 2019 and early 2020, the annual mean BBAOD in 2020 accounts for around 50 % of the total AOD in each region. Compared to the global mean, biomass burning accounts for only around 12 % of the total AOD. The regions are as follows: western US (-125--115° E, 30--50° N), central Africa (7--29° N, -13--6° E), southeast Australia (140--180° E, -45--30° N), northeast Siberia (90--175° E, 55--80° N), southern Amazonia (-65--55° E, -30--10° N).



Region	Latitude range (° N)	Longitude range (° E)	Total 2020 BC+OC BBA emission (Tg)	Mean 2020 AOD FIRE_DM	Mean 2020 BBAOD FIRE_DM
Western US	30, 50	-125, -115	1.16	0.11	0.060
Southeast Australia	-45, -30	140, 180	0.711	0.12	0.018
Northeast Siberia	55, 80	90, 175	3.61	0.11	0.055
Central Africa	-20, 5	8, 38	3.79	0.46	0.24
Southern Amazonia	-30, 0	-70, -50	2.71	0.22	0.10
Global	-90, 90	-180, 180	18.1	0.13	0.016

Table 2: Regions of analysis used in this study, with latitudinal and longitudinal range, total BC+OC BBA emission from 2020 (from GFED4.1s), annual mean AOD from 2020 (from FIRE_DM simulation), and annual mean BBAOD from 2020 (also from FIRE_DM simulation).

3 Results and discussion

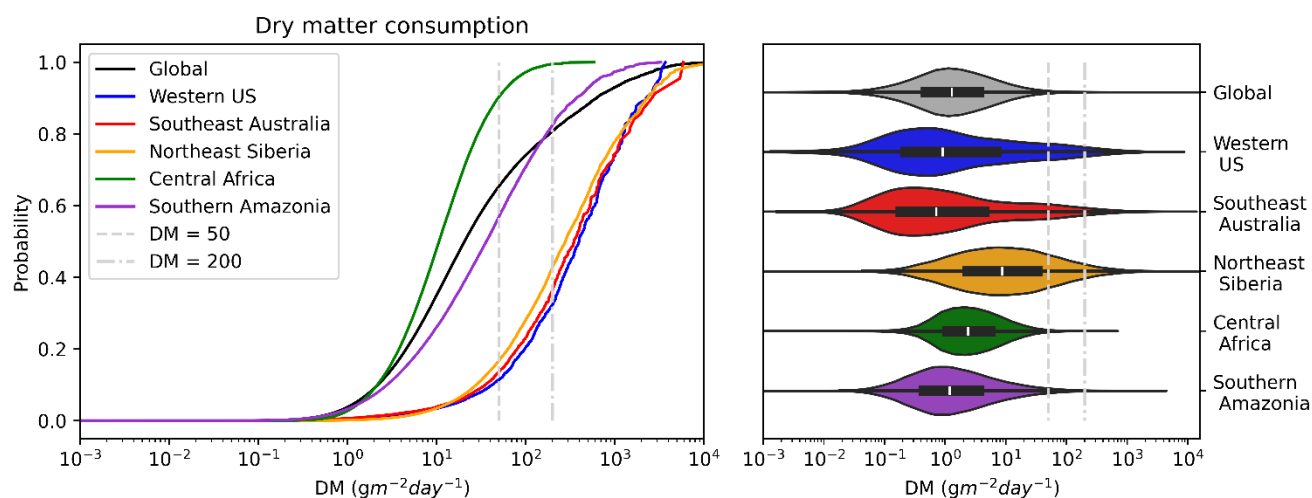
3.1 GFED4.1s aerosol emissions as a function of dry matter consumption

Figure 3 shows cumulative distribution and probability distribution functions for biomass burning aerosol emissions (BC + OC) as a function of the daily pixel-level DM estimated by GFED4.1s during 2020. These have been evaluated for the emissions both globally (black line) and for various fire-dominated regions including Western US (blue), southeast Australia (red), central Africa (green), northeast Siberia (orange), and southern Amazonia (purple). A clear separation is seen between results for regions that included notable extreme fire events during 2020 (northeast Siberia, SE Australia and western US), and the curves for southern Amazonia and central Africa. The extreme fire event regions have a higher proportion of emissions coming from pixels with greater DM per m² (which indicates larger fire and/or fuel load), while southern Amazonia and central Africa have a higher proportion of emissions from smaller values of DM per m² (indicating most emissions are from smaller fires and/or fires with lower fuel load per m²). The curves for southern Amazonia and central Africa more closely resemble the global distribution, though the global distribution is broader and illustrates the huge range of DM that is consumed by detectable fires, within GFED pixels. It is worth noting that spatially extensive fires have been shown to feature in Savanah regions (Andela et al., 2017) as well as in those regions we identify as “extreme fire regions” in our analysis. Half of global emissions originate from grid cells emitting less than 20.6 gm⁻² each day. In central Africa, which contributes the largest percentage of global biomass burning emissions, half of the emissions originate from cells



emitting less than 10.7 gm^{-2} per day. However, in the western US region, half of the emissions originate from cells emitting 400 gm^{-2} per day or greater.

275 As introduced in section 2.2, in this study we have devised a novel method for scaling biomass burning OC and BC emissions based on the mass of daily dry matter (fuel) consumption per m^2 from individual grid cells. This aims to scale up emissions in circumstances where fires may be less detectable, due to the fires either having a limited burned area and/or limited rate of fuel combustion per area, both of which would limit the radiative heat output of the fire. It assumes that grid cells with high daily dry matter include large and/or intense fires that are more readily detectable via their heat signature or
280 burned area and therefore do not need scaling to compensate for detection issues. This approach may also account for the effect of fuel consumption rate on EFs, though this effect is far less well documented in the literature than the burned area underestimate. To what degree either affects the need for scaling is beyond the scope of this paper and will require further study. Based on the cumulative distribution functions in Fig. 3 we identify suitable DM thresholds for the DM-based scaling method that enable emissions from most pixels to be scaled, except those from very intense or large fires. With a lower limit of $50 \text{ gm}^{-2}\text{day}^{-1}$, and an upper limit of $200 \text{ gm}^{-2}\text{day}^{-1}$, 65.3 % of 2020 global emissions continue to be scaled by 2, with 80.7 % getting some scaling applied. In central Africa, 90.3 % of emissions continue to be scaled by 2, with 99.5 % still getting
285 some scaling applied. In the western US, only 11.3 % of emissions get scaled by 2, with 32.3 % getting some scaling applied. Other lower and upper limits were tested (10–100 and 100–500), but we found 50–200 to give the best compromise for both the September 2020 western US fires, and globally, which is particularly clear to see in the violin plots in Fig. 3.



290 **Figure 3: Cumulative distribution function of daily mean dry matter (fuel) consumption from biomass burning in 2020 (left). The black line represents the global probability. Regions of fire occurrence are shown in blue (western US), red (southeast Australia), green (central Africa), orange (northeast Siberia), and purple (southern Amazonia). To the right, violin plots show the probability distributions of each region. The white line shows the median value, and the black box shows the interquartile range. In both plots, grey vertical dashed lines represent the FIRE_DM scaling factor thresholds.**
295

3.2 Evaluation of modelled AOD for the Californian wildfire event in September 2020

3.2.1 AOD comparison with AERONET

The daily mean AOD at 550 nm at all 77 AERONET sites has been co-located and compared to the AOD from the three simulations (FIRE_1X, FIRE_2X, FIRE_DM) across the month of September 2020. The agreement between modelled and observed AOD varies among the sites, somewhat according to geographic region, as illustrated by Fig. 4. In this plot the coloured markers at the location of the AERONET sites indicate the (inverse) gradient of the linear regression fit between the daily mean AODs from the FIRE_1X simulation and the co-located AERONET AODs, for September 2020. Only sites with a positive r^2 value are shown. Sites coloured in yellow indicate a good fit between AERONET and FIRE_1X, whereas sites in dark blue better fit with FIRE_2X. A clustering of points is observed, with the AERONET sites in the north predominantly fitting the FIRE_1X simulation better and sites in the south mostly showing a better fit with FIRE_2X. More detailed comparisons between the observed and modelled AOD are shown in Fig. 5 from three of the AERONET sites that were selected due to their high observed AODs (indicative of thick smoke), and to illustrate different outcomes that arose in different parts of the continent.

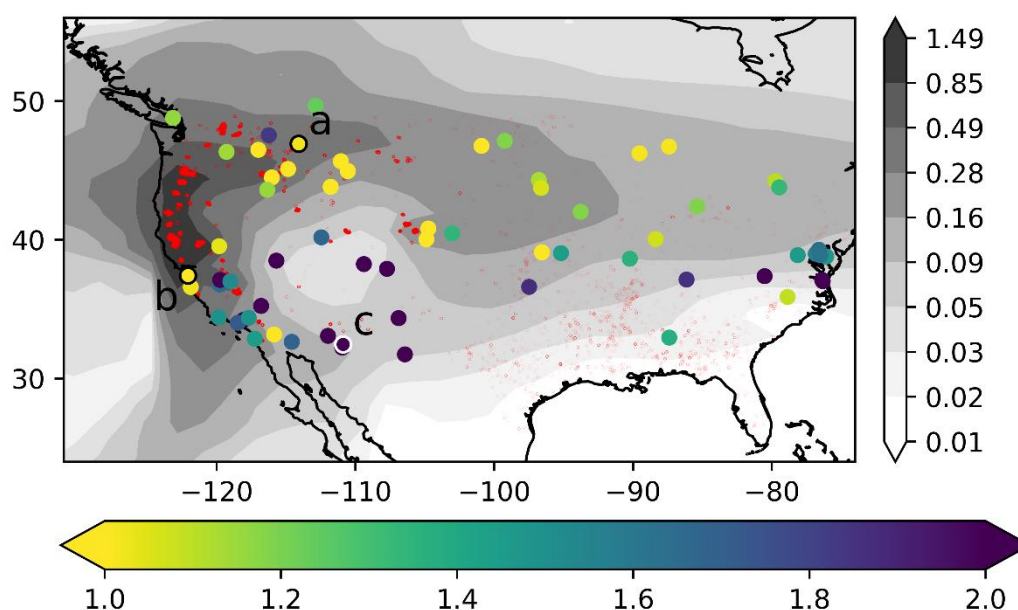


Figure 4: AERONET sites across North America for September 2020. The colours represent the inverse of the gradient of linear regression between daily mean AOD from AERONET and FIRE_1X simulation across September 2020. Sites coloured in yellow have a gradient of linear regression of 1 or lower, demonstrating a good fit with FIRE_1X. Sites coloured in dark blue have a gradient of 2 or higher, suggesting a better fit with FIRE_2X. Outlined locations a (Missoula), b (NASA Ames), and c (Catalina) are presented in Fig. 5. The mean AOD of September 2020 is shown as contours in grey, and a representation of the fire radiative power across the month is shown by red scatters, to provide an indicative location of the plume.



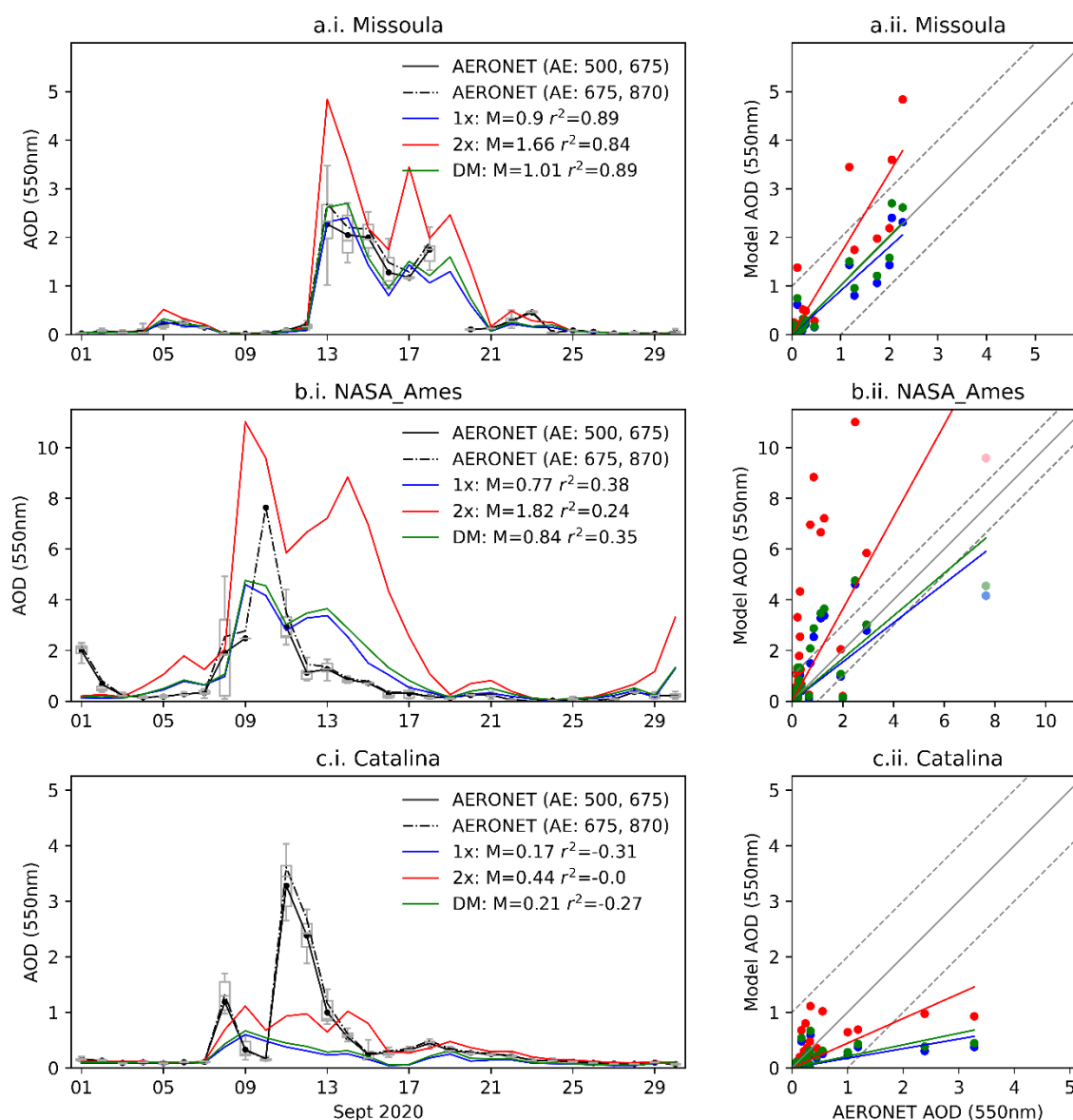
The AOD at Missoula remains below 0.5 until the 13th of September, when it rises steeply in both model simulations and observation, reaching a maximum of 2.3 in observations, before gradually reducing to 1.2 on the 17th. There is another peak on the 18th, of 1.7. After the 20th, the AOD remains below 0.5 until the end of the month, suggesting that the plume has fully
320 passed over this location. This trend is best captured by FIRE_DM, where the gradient of linear regression (forced through the origin) is 1.01, with an r^2 value of 0.89, giving a strong positive correlation. FIRE_1X also closely fits the observations (gradient = 0.9, r^2 = 0.89), also with a strong positive correlation. FIRE_2X follows the same trend but reaches a maximum AOD of 4.8 on the 13th, overestimating the BBA column loading by more than a factor of two, and having a gradient of linear regression of 1.66 (r^2 = 0.84). Clearly FIRE_2X, which has been used as the standard, overestimates AOD at this site
325 and the FIRE_DM scaling works best.

NASA_Ames is an AERONET site southwest of Missoula, closer to the location of the fires. In this example the time evolution of AOD in the model and observations don't match as well, but overall, the FIRE_DM simulation performs best at avoiding excessive overestimations and underestimations of AOD. The observed AOD is low until the 7th of September, then rose to 1.9 on the 8th, and to 2.5 on the 9th. The AOD on the 9th is overestimated by all simulations (FIRE_1X = 4.6,
330 FIRE_DM = 4.7), but most extremely by FIRE_2X, which has an AOD of 11.04 that day. The AERONET AOD at 500 nm was missing for the 10th of September and therefore an estimate of the 550nm AOD was extrapolated from the 675 and 870 nm values, giving an AOD of 7.6. To validate this method, we have plotted the AODs extrapolated from 675 and 870nm, for all available days alongside those interpolated from 500 and 675nm and find that for these three sites the two methods produced values within 0.4 (which was a +6.7 % difference). Therefore, we expect the very high 550nm AOD estimate of
335 7.6 for the 10th to be a reasonable guide value, despite difficulties with saturation at shorter wavelengths. In the simulations, the AOD on this day is overestimated by FIRE_2X (9.6) and underestimated by FIRE_1X and FIRE_DM (4.2 and 4.6). On the 11th, the AOD reduces to 2.9, which is best replicated by FIRE_DM (3.0). For the rest of the month, the AOD continues to decrease, being overestimated by all simulations. When we consider the month overall (Fig 5b. ii) we find that the best fit is given by FIRE_DM, with a gradient of linear regression of 0.84, and correlation coefficient of 0.35. The gradient of
340 FIRE_1X is 0.77 (r^2 = 0.38), followed by FIRE_2X (gradient = 1.82, r^2 = 0.24). The extrapolated AOD on the 10th of September (shown in faded colours in Fig 5b.ii) is included in linear regression calculations.

Catalina is located in the southeastern part of the plume. This example shows a case where none of the simulations performed well, indicating that emission scaling cannot address all sources of discrepancy in modelling the evolution of the smoke plumes from the Californian event. The AERONET AOD is initially low, then on the 8th there is a small peak of 1.2,
345 followed by a larger peak on the 11th of 3.3. The AOD steadily decreases and then remains low for the rest of the month. The correlation coefficients (-0.31 for FIRE_1X, -0.0 for FIRE_2X, and -0.27 for FIRE_DM) reveal that there is no positive correlation between model and observations. This is also shown in the timeseries where the peaks in simulations and observation are misaligned, and with a maximum modelled AOD of 0.60, 1.1 and 0.67 for FIRE_1X, FIRE_2X, and FIRE_DM, respectively. The modelled plume appears to be largely missed here, explaining why the southern part of the
350 plume is underrepresented by FIRE_1X (as indicated by blue dots in Fig 4). However, the FIRE_2X simulation is also



unable to capture the scale of the AOD at this point location, which would suggest insufficient transport of the plume across the southern region. This could either be through difficulty in reproducing or resolving the precise dynamical flow patterns involved, or due to very weak or missing emissions in the southern region that cannot be rectified through emissions scaling.



355 **Figure 5: Aerosol optical depth in three locations for September 2020 (left-hand panels in a–c, regions outlined in Fig. 4). i.**
Timeseries with observational AERONET data shown in black, with black dots representing the daily mean AOD. Grey boxplots
represent the median, interquartile range, minimum and maximum AOD of the AERONET data across the day. Model simulation
FIRE_1X shown in blue, and FIRE_2X shown in red. (a–c). ii. Data represented as scatter plots with linear regression (forced
through the origin). The gradient (M), and coefficient of determination (r^2) are shown for each plot. The three points in faded
 360 **colours in b.ii represent the extrapolated AOD on the 10th of September, which are used in linear regression calculations.**
Gradients calculated here are the inverse of those in Fig. 4.



These three cases exemplify a range of outcomes and illustrate that the DM scaling method in general reduces excessive overestimations of AOD from these extreme fires but cannot reconcile or resolve all errors in the modelling of the AOD plumes. More generally, disparities between model AOD and point observations can arise for various reasons, including errors in the estimated emissions from different fuel sources and fire regimes i.e. smouldering or flaming combustion, or the potential underestimation of burned area owing to either sub-pixel fires or obscuration of burned areas by overlying vegetative canopies. Using the dry matter-based scaling approach somewhat compensates for the latter, particularly when it comes to larger scale integration e.g. comparisons with Suomi VIIRS Deep Blue in section 3.2.2, and evaluation of other wildfire regions at a global scale in section 3.3.

Other sources of error may relate to the transport of the smoke and the representation of microphysical, chemical and optical properties that vary and evolve with time after emission. For instance, in a study of the physical and optical properties of aerosol from the 2020 Californian wildfires, Eck et al. (2023) identified two distinct plumes from fires on the 10th of September that were transported at different altitudes. A southern plume was identified between 5–10 km and the northern plume between 3 and 6 km. The southern plume had particles with larger fine mode radii, which Eck et al. (2023) suggested could have been due to variations in fire characteristics and aging and transport processes. UKESM uses a common initial particle size distribution for all biomass burning aerosol emissions and does not include the chemical ageing, condensation or evaporation of organics, limiting the variability in physical, chemical and optical properties that can be reproduced.

It is interesting to note that for each of the sites, the FIRE_2X AOD is not necessarily twice the FIRE_1X AOD. This is because the additional absorption in FIRE_2X can lead to an increase in the altitude of the BBA plume. This feature has been recognised before in studies examining climate responses to black carbon aerosols within models that are nudged to reanalyses (Johnson and Haywood, 2023). Despite the horizontal components of wind fields being quite tightly constrained by the nudging procedure, the vertical component of wind-speed is not and the absorption and self-lofting in the 2X simulations exceeds that in the 1X simulations leading to a higher altitude aerosol plume where the windspeeds differ. Thus, although the advection of the plume between the 1X and the 2X cases is similar, it is not identical.

3.2.2 AOD comparison with Suomi VIIRS Deep Blue

The mean AOD during September 2020 across North America is plotted in Fig. 6 for the FIRE_1X, FIRE_2X, and FIRE_DM simulations and satellite observations from Suomi VIIRS Deep Blue algorithm. The spatial distribution of aerosol is similar across observation and all three simulations, with the highest AOD occurring along the west coast, correlating with the locations of fires, as shown in Fig. 2. The smoke plume takes an approximate hourglass-shaped distribution, with an upper area of smoke spanning between 40–50° N, and -160–110° E, and a lower area between 15–30° N, and -120–100° E. The box drawn on each plot outlines the area (-125–115° E, 30–50° N) which is analysed further, as this is where the majority of the fires occurred and AOD is highest. The September mean AOD in this area is 0.42 in FIRE_1X, 0.89 in FIRE_2X, 0.49 in FIRE_DM, and 0.46 from the VIIRS Deep Blue retrieval.

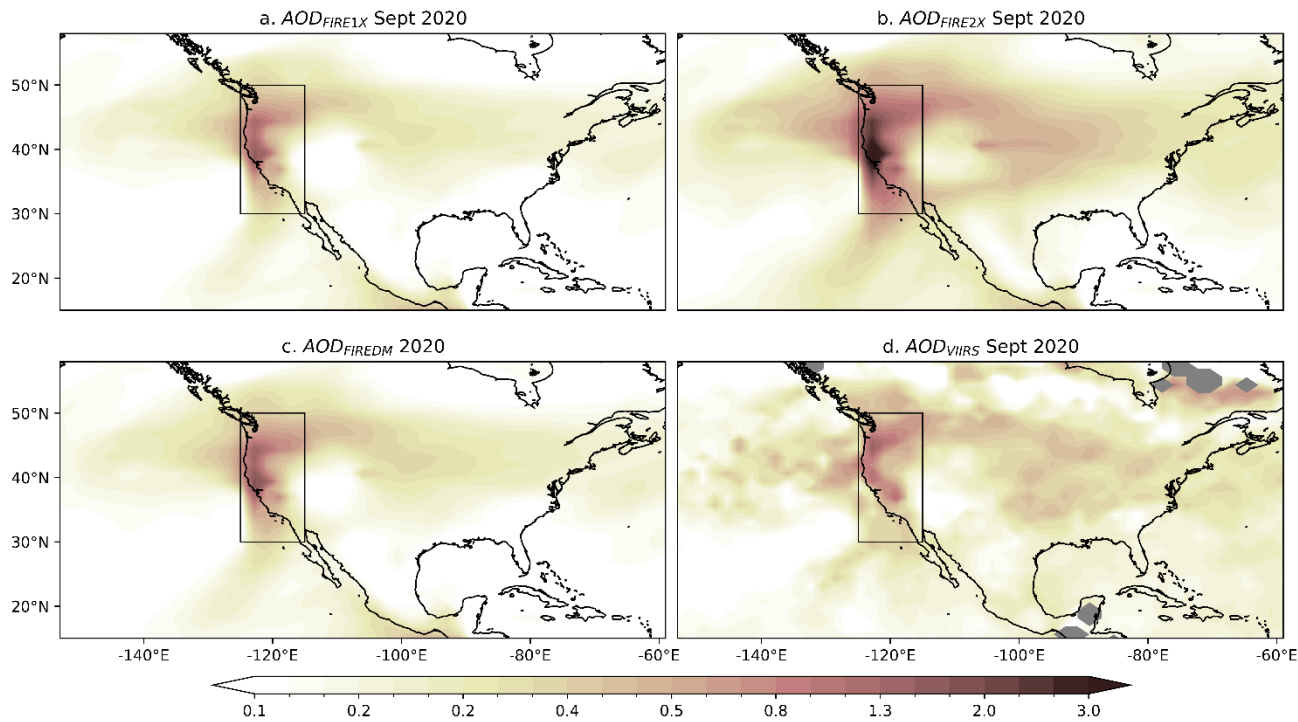


Figure 6: Mean Aerosol optical depth for September 2020. a. AOD from simulation FIRE_1X, using unscaled emissions. b. AOD from simulation FIRE_2X, emissions scaled by 2. c. AOD from Suomi VIIRS Deep Blue.

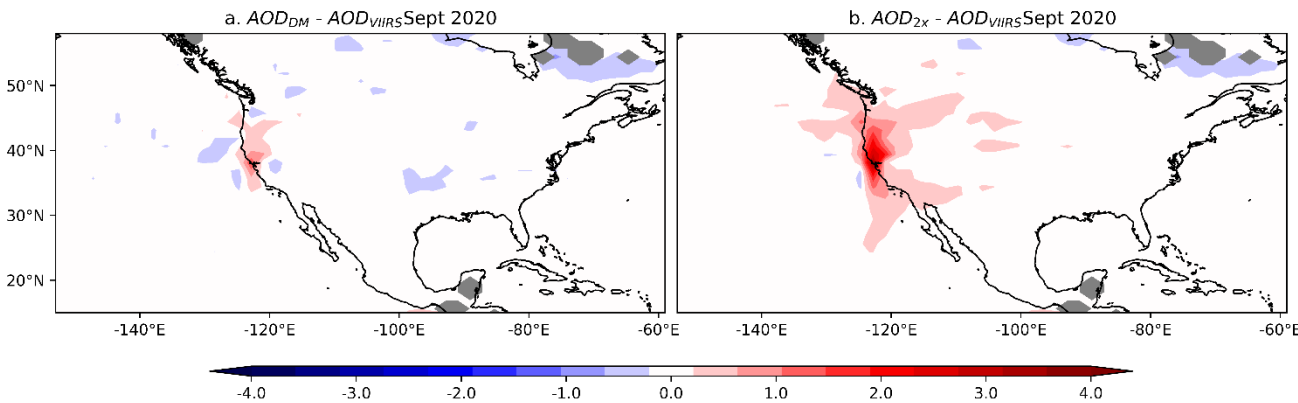


Figure 7: Difference between observation and model, September mean AOD a. Difference between FIRE_DM and VIIRS DB. b. Difference between FIRE_2X and VIIRS DB. Blue represents areas where the model simulation is underpredicting the AOD, red represents areas where the AOD is being overestimated.

Figures 7.a and 7.b show the difference in September mean AOD between FIRE_DM and VIIRS, and FIRE_2X and VIIRS, respectively. FIRE_DM appears to underestimate the AOD in some areas (Fig. 7.a), by up to 1, and in a small area near the



405 centre of the fires, overpredicts AOD by up to 1.4. However, FIRE_2X overpredicts the AOD by up to 3.7 at the location of the fires (Fig. 7.b). The comparison shows that applying the DM-based scaling method in FIRE_DM substantially limits the overestimation of AOD, relative to FIRE_2X, in the region where the modelled plume from the extreme fires contributed most significantly to monthly mean AOD, but does not cause large underestimation biases elsewhere. The difference between FIRE_1X and VIIRS DB is not depicted here but shows a similar distribution to 7.a (FIRE_DM), with a slightly
410 smaller area of overprediction, and larger area of underprediction.

Figure 8 shows a timeseries for the daily mean AOD averaged across the small region outlined in Fig. 6, for the month of September. The AOD peaks at 1.34 on the 12th of September in the observations, reaching values of 1.37, 2.54 and 1.52 in simulations FIRE_1X, FIRE_2X and FIRE_DM on this day, respectively. The peak for the FIRE_1X and FIRE_DM simulations is on the 13th of September, reaching values of 1.52 and 1.70. A second peak in observations occurs on the 17th
415 of September at 1.08, which is 0.94, 2.28, 1.12 in FIRE_1X, FIRE_2X and FIRE_DM. These peaks are well captured by FIRE_1X, where the simulated AOD is +2.2 % (12th Sept) and -12.8 % (17th Sept) of the observed value. Respective numbers for FIRE_DM are +13.7 % and +3.6 %, and for FIRE_2X, +89.3 % and +111.6 %, almost doubling and then more than doubling the AOD. The results indicate the best agreement between observed and modelled AOD when emissions are not scaled, and that the DM-based approach aligns closely with the unscaled results and the observations, particularly
420 preventing excessive overestimation of peak AOD values during the intense smoke event in the middle of the month.

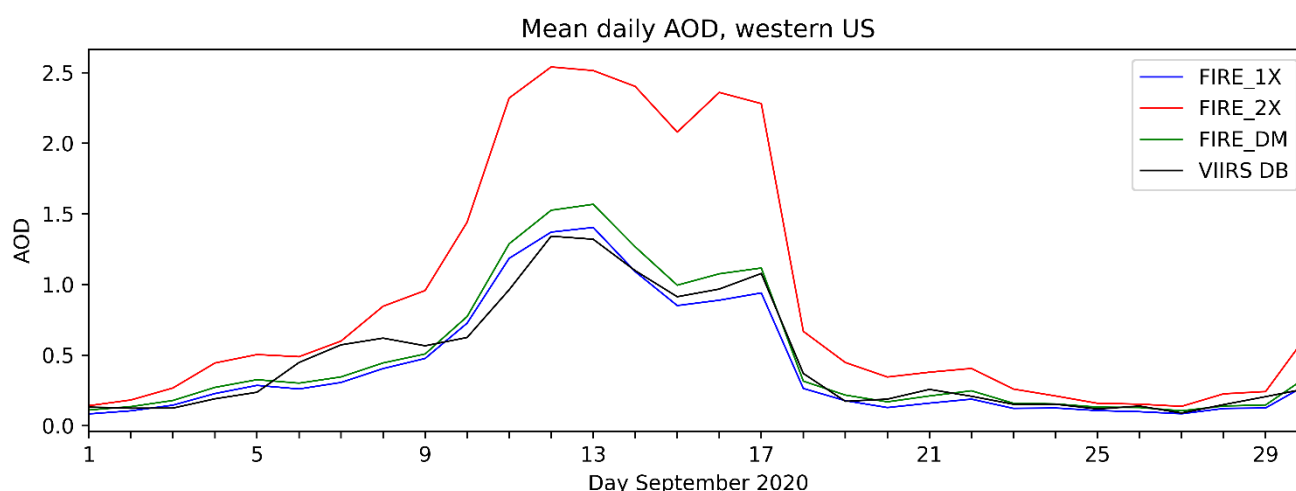


Figure 8: Area weighted daily mean AOD for region in western US, bounded by -125–115° E, 30–50° N, as marked in Fig. 6 by black rectangle. The black line is observational data from Suomi VIIRS Deep Blue, blue is the FIRE_1X simulation, red is the FIRE_2X simulation, and green is FIRE_DM simulation.

425

To provide a more statistical evaluation of the AOD differences, Fig. 9 shows scatter plots of daily mean AOD in September for the small region outlined in Fig. 6 from the simulations and the co-located VIIRS DB observations. To eliminate data points unlikely to be affected by biomass burning smoke, these data were screened to include only points with carbon



monoxide total column density greater than 100 ppbv (section 2.3). The linear regression fit is forced through the origin to
 430 derive the gradient (M), indicating the proportionality of the relationship between the observed and modelled AODs,
 whereby an M value of 1 would denote a one-to-one agreement. The gradient of linear regression closest to 1 is given by
 FIRE_DM, with a gradient of 1.001, followed by gradients of 0.894 for FIRE_1X, and 1.756 for FIRE_2X. The coefficient
 of determination (r^2) measures the correlation of the model data against the observations, with a value (range is 0 to 1)
 closest to one representing a perfect correlation/fit. From best fit to worst fit, the r^2 values are 0.484 (FIRE_DM), 0.481
 435 (FIRE_1X), and 0.432 (FIRE_2X). FIRE_DM has the strongest correlation, with linear regression closest to one.

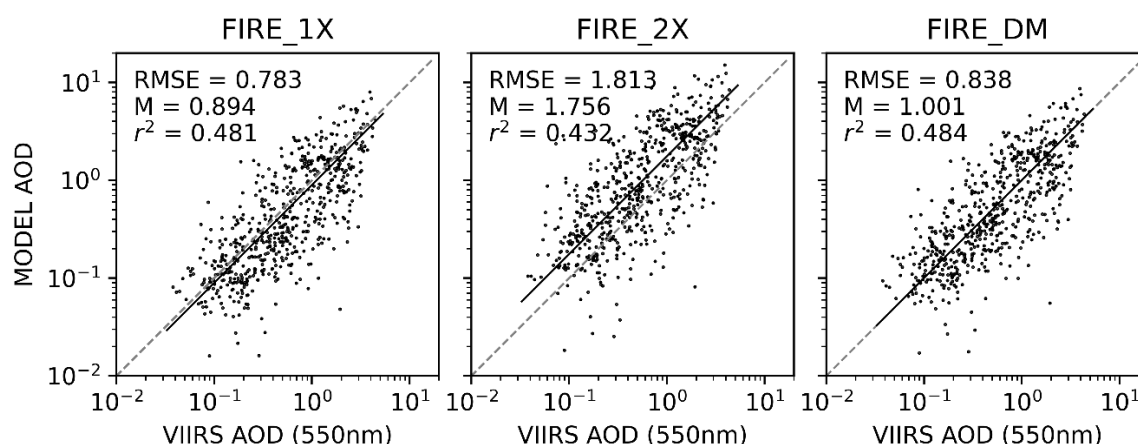


**Figure 9: Scatter plots of the carbon monoxide screened AOD ($\text{CO} > 100$ ppbv) in the western USA, for September 2020. VIIRS
 Deep Blue AOD against a. FIRE_1X b. FIRE_2X c. FIRE_DM. In each plot the line of best fit forced through the origin is drawn,
 the gradient of which (M) is displayed in the top left. The root mean square error (RMSE) and coefficient of determination (r^2) are
 440 also shown here.**

The root mean squared error (RMSE) based on the differences between modelled and observed AODs is also shown in Fig.
 9, providing a means of quantifying the degree of scatter or discrepancy. The lowest RMSE values are for the FIRE_1X and
 FIRE_DM simulations (0.783 and 0.838, respectively, compared to 1.813 for FIRE_2X). A further indicator, the mean
 445 absolute error (MAE) was also calculated for the simulations against observations (though not shown in Fig. 9). From best to
 worst, MAE values are calculated as 0.48 (FIRE_1X), 0.51 (FIRE_DM), and 1.03 (FIRE_2X). Finally, the concordance
 correlation coefficient was calculated, which evaluates the agreement between two variables by measuring the variance from
 the concordance line (the 45° line through the origin) (Lin, 1989). Values range from -1, giving perfect disagreement, to 1,
 giving perfect agreement. From best to worst, these are 0.68 (FIRE_1X), 0.67 (FIRE_DM), and 0.42 (FIRE_2X). Overall,
 450 these statistical evaluations confirm that avoiding scaling emissions by a factor of 2 improves the agreement between
 modelled and VIIRS observations of AOD for instances when the aerosol column was likely dominated by wildfire smoke.
 In these comparisons, over the region strongly affected by the extreme fire event FIRE_DM performs similarly well to
 FIRE_1X, offering a marginal improvement in the gradient of the linear regression fit and small, mixed differences across
 the range of other statistical measures evaluating the degree of correlation and scatter.



455 3.3 Evaluation of the modelled AOD for other wildfire regions and at the global scale

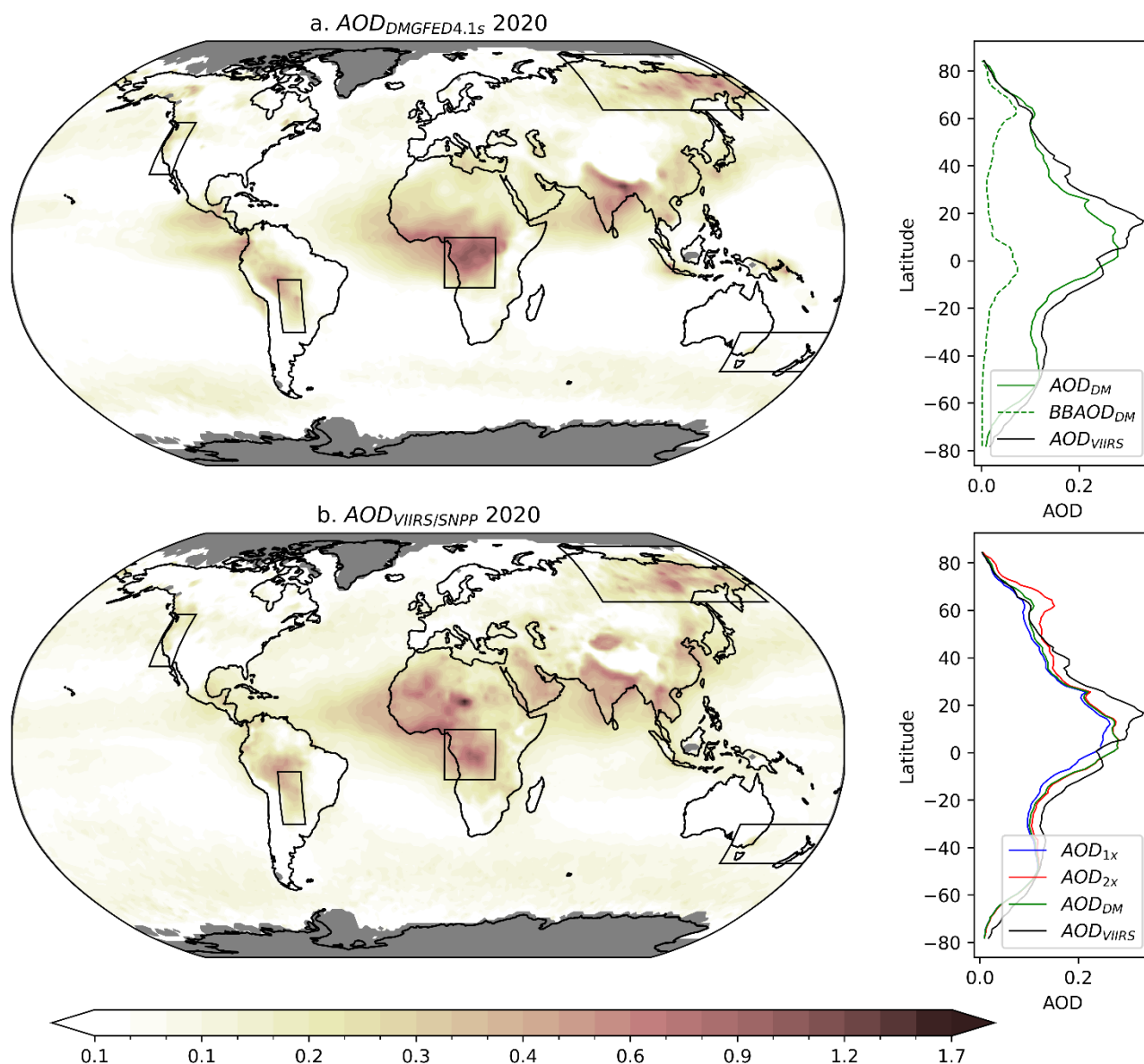


Figure 10: Annual mean AOD for 2020 a. FIRE_DM simulation, using dry matter consumption dependent scaling. b. Suomi VIIRS Deep Blue (DB). The latitudinal AOD is plotted alongside, where the black line represents VIIRS DB, the green line collocated FIRE_DM and the dashed line represents the biomass burning AOD (BBAOD), calculated by subtracting the NO_FIRE simulation from FIRE_DM. In the second plot, the blue line represents collocated FIRE_1X, and the red line collocated FIRE_2X. Regions marked by black boxes are: western US (-125–115 ° E, 30–50° N), central Africa (7–29° N, -13–6° E), southeast Australia (140–180° E, -45–30° N), northeast Siberia (90–175° E, 55–80° N), southern Amazonia (-65–55° E, -30–10° N).



In Figure 10, we evaluate how well the modelled AOD compares to satellite observations, focussing on the FIRE_DM simulation in regions (drawn as boxes in Fig. 10) and latitude zones (shown in zonal mean side figures) where biomass burning emissions strongly contribute to annual mean AOD. Of the five regions that are characterised by strong wildfire activity, central Africa, southern Amazonia and northeast Siberia present the strongest peaks in regional AOD in both the model (FIRE_DM) and observations (VIIRS DB). Peak values and spatial distributions in those regions are reassuringly similar in the two maps (Fig. 10a & b) and in the comparison of zonal mean AODs from FIRE_DM and VIIRS (green and black lines). To aid the interpretation, the zonal mean plot shows also the contribution of biomass burning to the AOD in the FIRE_DM simulation (labelled as BBAOD_{DM}). This component is calculated as the AOD difference between the FIRE_DM and NOFIRE simulations. What this reveals is that at least half of the modelled AOD between 60 – 80° N is attributable to wildfire emissions, whereas BBAOD is a minor fraction elsewhere, albeit with a secondary peak in the deep tropics. The zonal mean plot in Fig. 10b furthermore shows how AODs are overestimated in FIRE_2X (red line) in northern high latitudes, as the contribution from smoke becomes much stronger than in FIRE_DM and too strong relative to the observations. Alternatively, FIRE_DM and FIRE_2X have virtually the same zonal mean AOD across the tropics (-30–30° N), where the contribution from BBAOD is about the same and in both cases lead to a peak in modelled AODs at the equator that approximately match the observed AOD. The contribution of Saharan mineral dust to AOD in the tropics appears underestimated in these simulations, which likely explains why observed AOD reaches higher peak AOD values slightly further north than the models.

The AOD timeseries for selected regions (western US, southeast Australia, northeast Siberia, central Africa, and southern Amazonia) are plotted in Fig. 11. In each plot, the most significant three-month period for biomass burning is plotted. Fig. 11a shows the western US region from the 1st of August to the 1st of November. On the 20th of August, the AOD reaches 0.66, which is not fully captured in any of the simulations. Later in the period, on the 1st of October, there is another small peak (0.30), which is overestimated by all simulations, in particular, FIRE_2X (0.79). The month of September is discussed in detail in section 3.2.2.

January 2020 was the peak month for the Australian Black Summer fires. Figure 11 shows that the daily mean AOD observed by VIIRS for the box covering southeast Australia (see Fig. 10) peaked at a value of 0.83 on 4th January, most accurately modelled by FIRE_1X (0.91), where FIRE_DM is 1.1 and FIRE_2X AOD is 1.8. The maximum observed value in the region was 4.3. A second peak of 0.51 occurs in the middle of the month, on the 14th of January. This is best modelled by FIRE_2X (0.50), with the other two simulations underestimating. As there was significant burning towards the end of 2019 in this region, we have additionally compared the November and December 2019 timeseries. We found two peaks in the AOD, the first on the 6th of December (0.41), which was best modelled by FIRE_1X (0.44) then FIRE_DM (0.49), with FIRE_2X overestimating (0.82). On the 19th of December, the AOD was 0.34, also best modelled by FIRE_1X (0.35), followed by FIRE_DM (0.40), and overestimated by FIRE_2X (0.63).

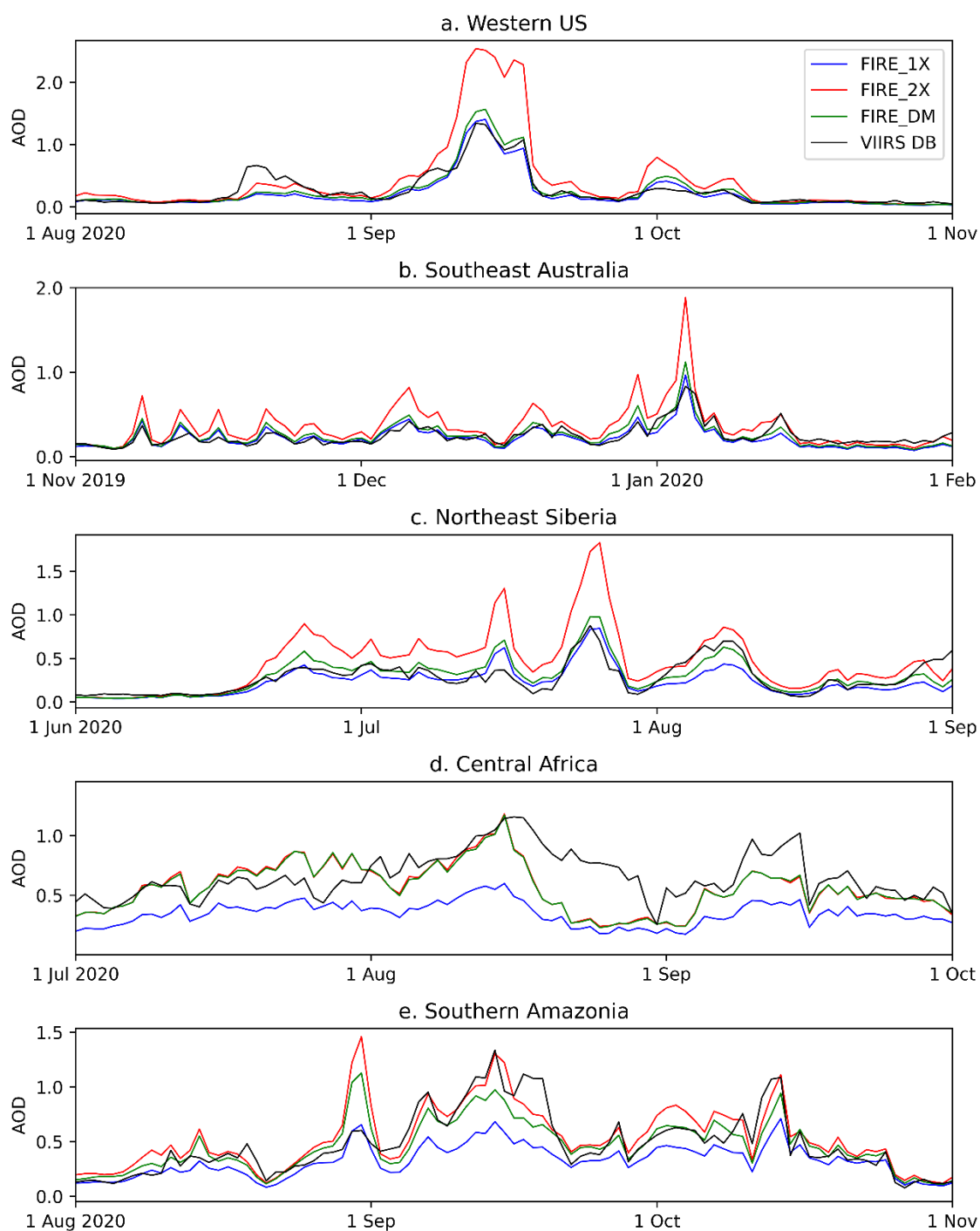


Figure 11: Area weighted daily mean AOD for five regions of biomass burning, shown in Fig. 10 with boxes outlined in black. The black line is observational data from Suomi VIIRS Deep Blue, blue is the FIRE_1X simulation, red is the FIRE_2X simulation, and green is FIRE_DM simulation.



500

The northeast Siberian extreme fire event took place throughout June, July and August 2020. The maximum observed AOD by VIIRS DB was 4.9, the highest daily mean AOD was 0.88 on the 25th of July. This is best modelled by FIRE_1X (0.83), and FIRE_DM (0.98), and is overestimated by FIRE_2X (1.7). A second peak of 0.7 on the 9th of August is best modelled by FIRE_DM (0.6).

505 There is consistent biomass burning in central Africa throughout July, August and September. The day with the highest AOD was the 16th of August, at 1.2. The AOD of FIRE_2X (0.89) and FIRE_DM (0.88) are similar for this day, with FIRE_2X just slightly higher. On the day before, the 15th, the observed AOD is 1.2. This is met by FIRE_2X (1.2) and FIRE_DM (1.2) simulations. This demonstrates the model's ability to capture the extent of the biomass burning aerosol, though the discrepancy between observed and modelled AOD from mid-August to early September suggests that there may be other
510 non-biomass burning contributions which are not so well captured, such as dust. Other potential explanations include missing emissions from GFED, or the aerosol processes in the model causing early deposition.

Wildfires in southern Amazonia occurred throughout August, September and October. The maximum daily mean AOD was 1.3, on the 14th of September, which was best modelled by FIRE_2X (AOD = 1.3). Another high daily mean AOD of 1.10 occurred on the 14th of October, which was also best modelled with FIRE_2X (1.1), followed by FIRE_DM (0.94).
515 FIRE_1X only had an AOD of 0.71. On the 1st of September, both FIRE_2X (1.5) and FIRE_DM (1.1) predict a very high AOD, which is not observed by VIIRS (0.60). This day is better modelled by FIRE_1X (0.66). The mean AODs for this each 3-month period regionally are presented in Table 3. FIRE_DM consistently reproduces the most accurate AOD for these regions and times when comparing to VIIRS DB satellite retrievals.

Region	VIIRS DB 3-monthly mean AOD	FIRE_1X 3-monthly mean AOD	FIRE_2X 3-monthly mean AOD	FIRE_DM 3-monthly mean AOD
Western US	0.27	0.22	0.42	0.25
Southeast Australia	0.24	0.22	0.36	0.25
Northeast Siberia	0.28	0.24	0.47	0.30
Central Africa	0.67	0.35	0.57	0.57
Southern Amazonia	0.48	0.33	0.54	0.47

520 Table 3: Mean AODs of 3-month period shown in Fig. 11 for each region of analysis.



Figure 12 shows carbon monoxide screened scatter plots of global regions of biomass burning (boxes marked on map in Fig. 10). Overlapping points are represented by the colour bar, where red shows the highest density of points, and dark purple shows only one point. The closest gradient of linear regression is given by FIRE_2X (1.039) and is closely followed by FIRE_DM (0.849), and then FIRE_1X (0.601). However, FIRE_2X has a root mean square error (RMSE) of 0.706, and r^2 value of 0.307, suggesting a larger amount of variation than FIRE_DM (RMSE = 0.520, r^2 = 0.357). The mean absolute errors (MAE), from best to worst, are 0.3 (FIRE_DM) and 0.3 (FIRE_1X), then 0.37 (FIRE_2X). The concordance correlation coefficients (CCC), from best to worst, are 0.63 (FIRE_DM), 0.55 (FIRE_1X), 0.54 (FIRE_2X).

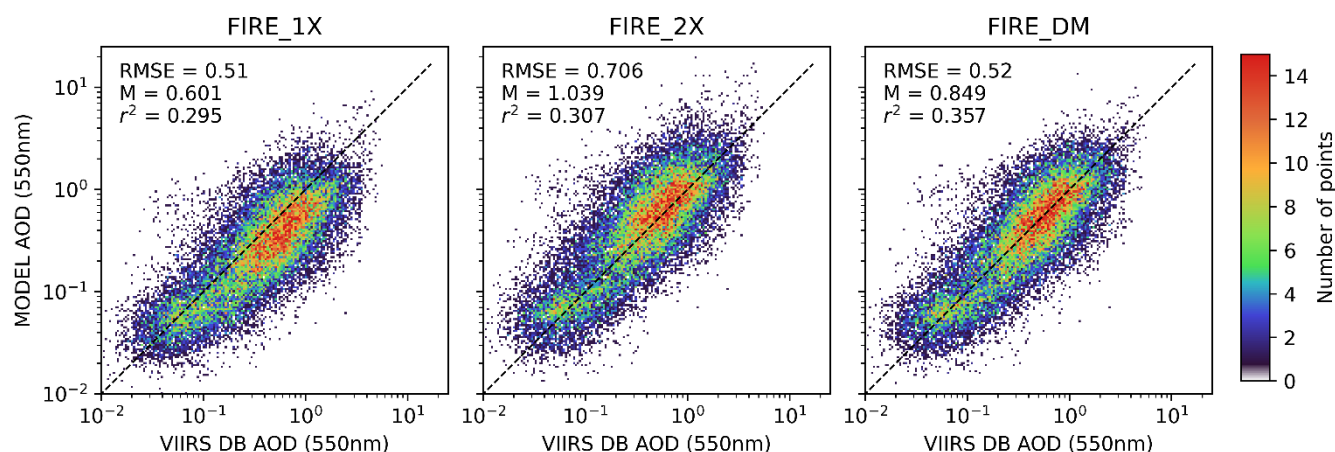


Figure 12: Scatter plots of the carbon monoxide screened AOD (CO>100 ppbv) in the selected five regions (boxes in Fig. 10) where biomass burning was a strong source of aerosol in 2020. Colour bar represents overlapping points, where red shows the highest density of points, and dark purple shows just one point. VIIRS Deep Blue AOD against a. FIRE_1X b. FIRE_2X c. FIRE_DM. In each plot the line of best fit forced through the origin is drawn, the gradient of which (M) is displayed in the top left. The root mean square error (RMSE) and coefficient of determination (r^2) are also shown here.

In agreement with Johnson et al. (2016), we find that scaling emissions is still essential to reduce errors between modelled and observed AOD in regions where BBA are a strong contributor to AOD. For instance, the FIRE_1X simulation particularly underestimated AOD in central Africa and southern Amazonia, whereas FIRE_DM and FIRE_2X performed better in those regions. However, FIRE_2X overestimated AOD in the other three regions (western US, southeast Australia, northeast Siberia) during times of intense fire activity. FIRE_DM shows a more skilful approach in that it applies a lower scaling in those three extratropical regions, especially at times when strong emissions lead to high peaks in AOD, whilst still addressing the low biases of AOD in central Africa and southern Amazonia. In doing so, FIRE_DM reduces the RMSE and increases r^2 relative to the FIRE_2X simulation, indicating improved agreement overall when assessing data from all five regions together in Fig. 12. FIRE_2X only outperforms FIRE_DM in limited instances, such in southern Amazonia during September (Fig. 11) but in other months, FIRE_DM provides a better fit than FIRE_2X in that region.



3.4 Global radiative forcing: The impact of emissions scaling

We estimate the clear-sky top-of-atmosphere (TOA) radiative forcing of biomass burning aerosols in 2020 for the three simulations applied to daily mean emissions. The monthly mean IRF's are plotted in Fig. 13, where the blue line is FIRE_1X, the red line is FIRE_2X, and the green line is FIRE_DM. In FIRE_1X, the annual mean IRF is -0.169 Wm^{-2} , in FIRE_2X, it is -0.338 Wm^{-2} , and in FIRE_DM, it is -0.251 Wm^{-2} . These differences in radiative forcing are approximately proportional to the differences in biomass burning aerosol optical depth (BBAOD), which are 0.009 (FIRE_1X), 0.020 (FIRE_2X), and 0.016 (FIRE_DM). For example, doubling GFED4.1s emissions approximately doubles the BBAOD, and by extension IRF. As this analysis shows, the emission scaling factor makes a significant difference to global annual mean radiation budget. Furthermore, due to the absorbing nature of biomass burning aerosol the atmospheric absorption and the IRF at the surface are several times greater than the TOA IRF, which emphasizes the potential climate impacts of accurately scaling their emissions.

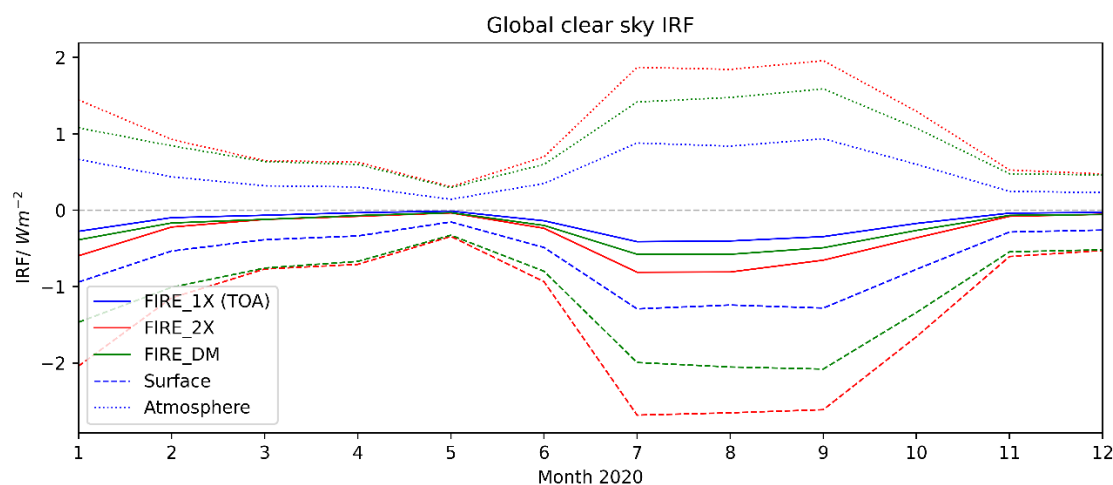


Figure 13: Clear sky (cloud free) top of atmosphere radiative forcing (solid line) of wildfires globally, for three simulations: FIRE_1X (blue), FIRE_2X (red), and FIRE_DM (green), for the year 2020. Dashed line is surface forcing, and dotted line is atmosphere forcing.

3.5 Radiative forcing: Benefits of using daily rather than monthly mean emissions

Since monthly mean emissions are more typically used in global climate simulations, this section examines the potential differences and benefits of employing daily mean emissions, in capturing the mean radiative effects of smoke aerosol and the extremes. We first evaluate how the choice between daily and monthly emission affects the radiation budget at the monthly timescale by comparing mean TOA shortwave IRF over the western US region for September. Using monthly mean emissions (FIRE_DM_MO) leads to a relatively similar TOA radiative impacts as using daily emissions (FIRE_DM), once results are averaged over the whole month (Fig. 14). Some differences in the geographic distribution are apparent and the



magnitude of IRF in the region around the extreme fires is somewhat weaker in FIRE_DM_MO. For instance, the average
570 IRF in the western US region was -6.70 Wm^{-2} (FIRE_DM) and -6.13 Wm^{-2} (FIRE_DM_MO) for clear-skies and -4.05 Wm^{-2}
(FIRE_DM) and -4.06 Wm^{-2} (FIRE_DM_MO) for the all-sky forcing. Peak values in this box were also slightly weaker in
FIRE_DM_MO. For example, the small area of positive all-sky IRF over the Pacific reached values of 16.8 Wm^{-2} in
FIRE_DM and only 11.5 Wm^{-2} in FIRE_DM_MO. This area of positive radiative forcing off the coast of California is due
575 around the California/Oregon border (40° N , -120° E) and a little different between the two simulations: -17.7 Wm^{-2} for
FIRE_DM, and -17.5 Wm^{-2} for FIRE_DM_MO.

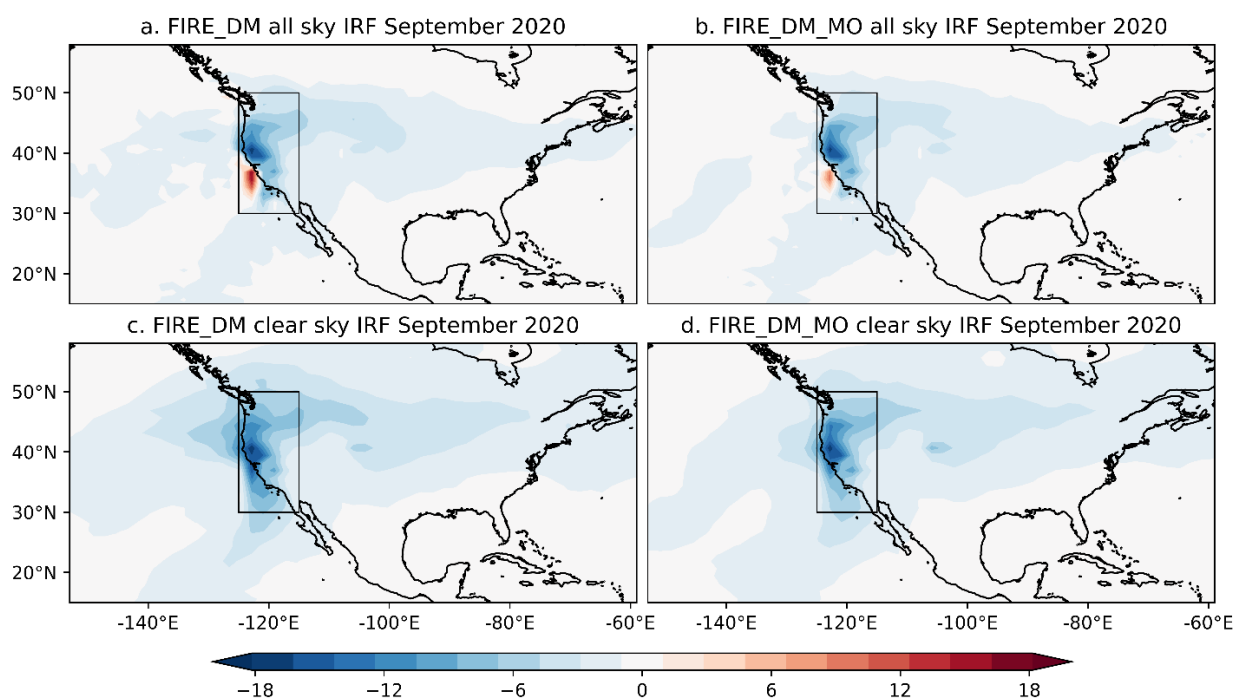


**Figure 14: Mean top-of-atmosphere shortwave instantaneous radiative forcing for September 2020, calculated as the difference
580 between FIRE_DM simulations and NOFIRE IRE. a. all-sky FIRE_DM (daily mean emissions) b. all-sky FIRE_DM_MO
(monthly mean emissions) c. clear-sky FIRE_DM d. clear-sky FIRE_DM_MO. The western US region is outlined by the black box
and consistent with previous figures and analyses spans -125 – -115° E and 30 – 50° N .**

The frequency of the individual grid cell all-sky IRF values in September for the Western US region outlined by the black
box in figures 14a–d is plotted in Fig. 15. The most common value for both the daily and monthly mean emissions is
585 between -5 – 5 Wm^{-2} , followed by -15 – 5 Wm^{-2} , and then -25 – 15 Wm^{-2} . The histogram illustrates the wider range of values
modelled by the daily simulation. The maximum all-sky IRF is 89.4 Wm^{-2} , as estimated using daily mean, whereas the
maximum for monthly mean simulation is only 49.5 Wm^{-2} . The strongest negative forcings are -48.0 Wm^{-2} in FIRE_DM,
and -28.7 Wm^{-2} in FIRE_DM_MO.



Figures 15b and c show the daily fluctuations of radiative effects in the two simulations for the same Western US region, for clear sky (b) and cloudy sky (c). In these plots, the green line represents the daily means simulation (FIRE_DM), and the purple line represents the monthly means simulation (FIRE_DM_MO). On the 12th of September, FIRE_DM exhibits the lowest clear-sky IRF of -17.4 Wm^{-2} , whereas this only reaches a minimum of -9.6 Wm^{-2} in FIRE_DM_MO. Simulating with daily mean emissions clearly increases the variability and peak magnitudes of radiative effects. However, as reported above, these differences average out over the month such that the September mean clear-sky IRFs in the outlined region is only 8.4 % weaker in the FIRE_DM_MO simulation and the all-sky IRF FIRE_DM_MO is 0.1 % greater in magnitude than FIRE_DM (i.e. very little difference).

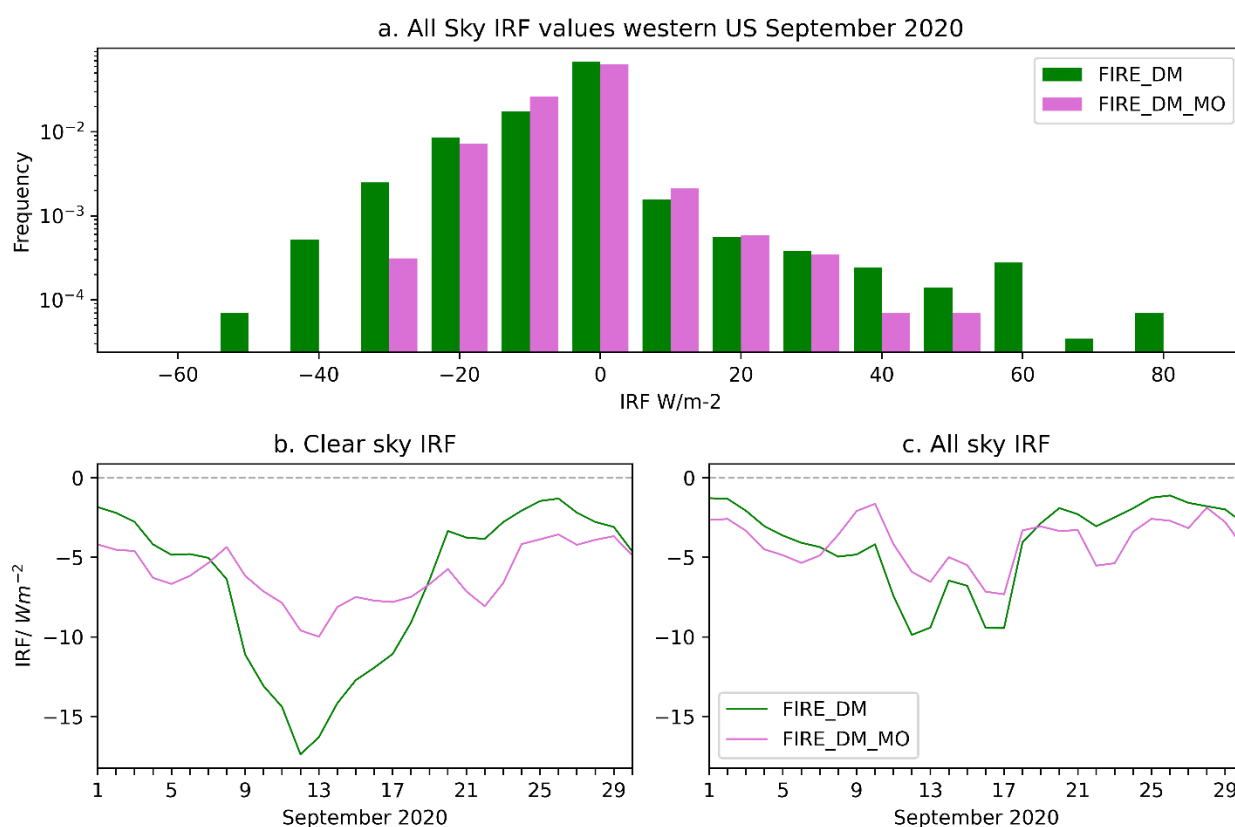


Figure 15: a. Frequency distribution of all-sky TOA IRF, for all grid cells in western US region, for September 2020. Results from the simulation with daily mean emissions (FIRE_DM) are shown in dark green, and results from the simulation with monthly mean emissions (FIRE_DM_MO) shown in purple. Also shown are time series of daily mean TOA IRF for September for the western US region for (b) clear sky and (c) all-sky.

The main result from this section is that when emissions are averaged into monthly means the variability and maximum strength of radiative effects are reduced. To capture the daily fluctuations in radiative effects of extreme wildfire events, on a local scale, daily mean emission would therefore be recommended. In addition, synchronising the timing of peak emissions



with the corresponding meteorological conditions may be important (since we have run these simulations with nudged winds) to predict the very high smoke AODs over the ocean and the distribution of underlying marine stratocumulus leading to much stronger positive all-sky aerosol IRF values. However, switching from monthly to daily emissions may have little impact on the mean radiative effect of BBA over longer timescales (monthly or longer) and on regional or global scales.

610 4 Conclusion

Extreme fire events, such as the Californian Wildfires in September 2020, make a significant contribution to global biomass burning aerosol emissions and their radiative impact, emphasising the need for these events to be accurately captured in climate models, alongside the contribution from other, seasonal fire activity (Johnson et al., 2016). In this study we explore two limitations in the modelling of these extreme wildfire events, the emissions scaling factor, and impact of using monthly
615 mean rather than daily mean emissions of organic and black carbon from GFED4.1s, evaluating this on a local as well as global scale.

We find that GFED4.1s is capable of capturing biomass burning aerosol emissions from extreme wildfire events which have large associated daily dry matter (fuel) consumption, but a 2x scaling is required to fully capture the contribution from fires with a lower fuel consumption which are more frequent globally. Based on this finding, we develop a unique method of
620 scaling GFED4.1s emissions based on the daily dry matter consumption per grid cell and find that it is able to represent observed AODs for the extreme Californian wildfire event, as well as improving agreement between modelled and observed AOD for other regions where wildfires with different levels of DM consumption contributed strongly to AOD. These included regions with boreal forest (northeast Siberia), temperate forest (southeast Australia) and those with a mixture of tropical forest and Savanah (central Africa and southern Amazonia).

The main implication of this study is that applying globally uniform scaling factors to wildfire emissions in global climate models can lead to excessive aerosol from wildfire events with larger and/or more intense fires. However, rather than varying the scaling according to identified regions our scaling approach identifies areas where GFED4.1s either under- or overestimates pyrogenic aerosol emissions based on the detected intensity of fire activity. This achieves the goal of leaving emissions unscaled where the burned area and dry matter consumption was large and well captured in the emission product,
630 whilst maintaining the application of scaling in the more pervasive circumstance where fire activity (according to the fuel consumed per unit area) is present but less intense and therefore a higher proportion of emissions may go undetected. We found this selective scaling method outperformed the use of a single, universal scaling factor as in many previous studies (e.g. Marlier et al., 2013; Matichuk et al., 2008; Reddington et al., 2016; Johnson et al., 2024). The findings of this study can therefore be used to improve the fidelity of future simulations of extreme fire events.

Secondly, we found that the AOD and IRF associated with wildfire aerosol emissions increased proportionately with the
635 emitted mass of organic and black carbon when these were scaled by a factor of 2, underscoring the importance of accurately representing the magnitude of these emissions. This linearity of response was also apparent when comparing results from



simulations driven by daily or monthly mean emissions, in that the time resolution of the emissions had little impact on the monthly mean IRF at a regional or continental scales. In that comparison, the simulation with daily mean GFED4.1s emissions and the dry matter consumption-based scaling factor (FIRE_DM), were compared to the simulation where those emissions had been averaged over the month (FIRE_DM_MO). As expected, FIRE_DM_MO did not capture the same degree of temporal and spatial variability of IRF, or the magnitude of extreme values that are simulated by FIRE_DM. Therefore, daily emissions may offer some advantages over monthly means in accurately capturing localised extremes in AOD and radiative effects. However, these differences averaged out over the broader western US region when evaluated at the monthly timescale. This is somewhat surprising given the potential for non-linear processes or feedbacks between the aerosol mass burden and aerosol microphysical and radiative interactions. It could be that competing non-linear interactions such as the saturation of radiative effects with AOD, were not sufficiently important after averaging out over space and time or that various competing non-linear interactions cancelled. Similar conclusions were reached by de Graaf et al. (2014) for smoke aerosol over the SE Atlantic. Either way, it underlines that the foremost focus should be on capturing the magnitude of emitted mass as this relates to detectable characteristics of the fires and consumed fuel load.

Some important caveats should also be noted to aid the interpretation of the findings above and motivate future work. Firstly, our analysis focuses on evaluating pyrogenic AOD and its relationship to the emissions of BC and OC mass, and it is worth noting that the representation of AOD depends on many other factors besides the amount of aerosol mass emitted. The AOD for a given aerosol mass loading is determined by the specific extinction coefficient, which depends on the aerosol size distribution, chemical composition and humidification (e.g. Johnson et al., 2016; Petrenko et al., 2025). Transport and deposition are also key to the dispersal of plumes and evolution of aerosol mass over time. Thus, improvements in such processes, affecting aerosol mass and the microphysical, chemical and optical properties may be similarly important in reducing biases and scatter in comparisons of modelled and observed AODs. Secondly, further work is required to develop a deeper understanding of how and why the emissions from fires with smaller DM are apparently still underestimated with the methodology employed for GFED4.1s (at least for 2020). Further evaluations from a broader time period and including other recent extreme fire events (e.g. Chen et al., 2025) may be instructive to test the broad applicability of our findings. Furthermore, there is a need to determine whether this apparent need for selective scaling based on the DM (fuel consumption) points entirely to difficulties in detecting smaller and/or less intense fires, or if the emission factors themselves (the BC and OC emitted per kg of biomass consumed) vary with the magnitude of fuel consumed. For instance, the nature of the combustion (flaming versus smouldering) has a strong influence on emission factors, and this could vary with the characteristics of fires, including their size and/or intensity. Thus, variables such as fuel density, moisture content / flammability and fire weather conditions may be more fundamental in driving variability and biases in wildfire aerosol emissions. Further research is required to unpick such issues and aid the ongoing development of satellite-based fire emission products and their implementation in atmospheric models.



670 **Appendix A**

This study used level 2 AOD data from 77 AERONET sites across North America, selected based on data availability for the month of September 2020. The locations and names of these sites are shown in Fig. A1.

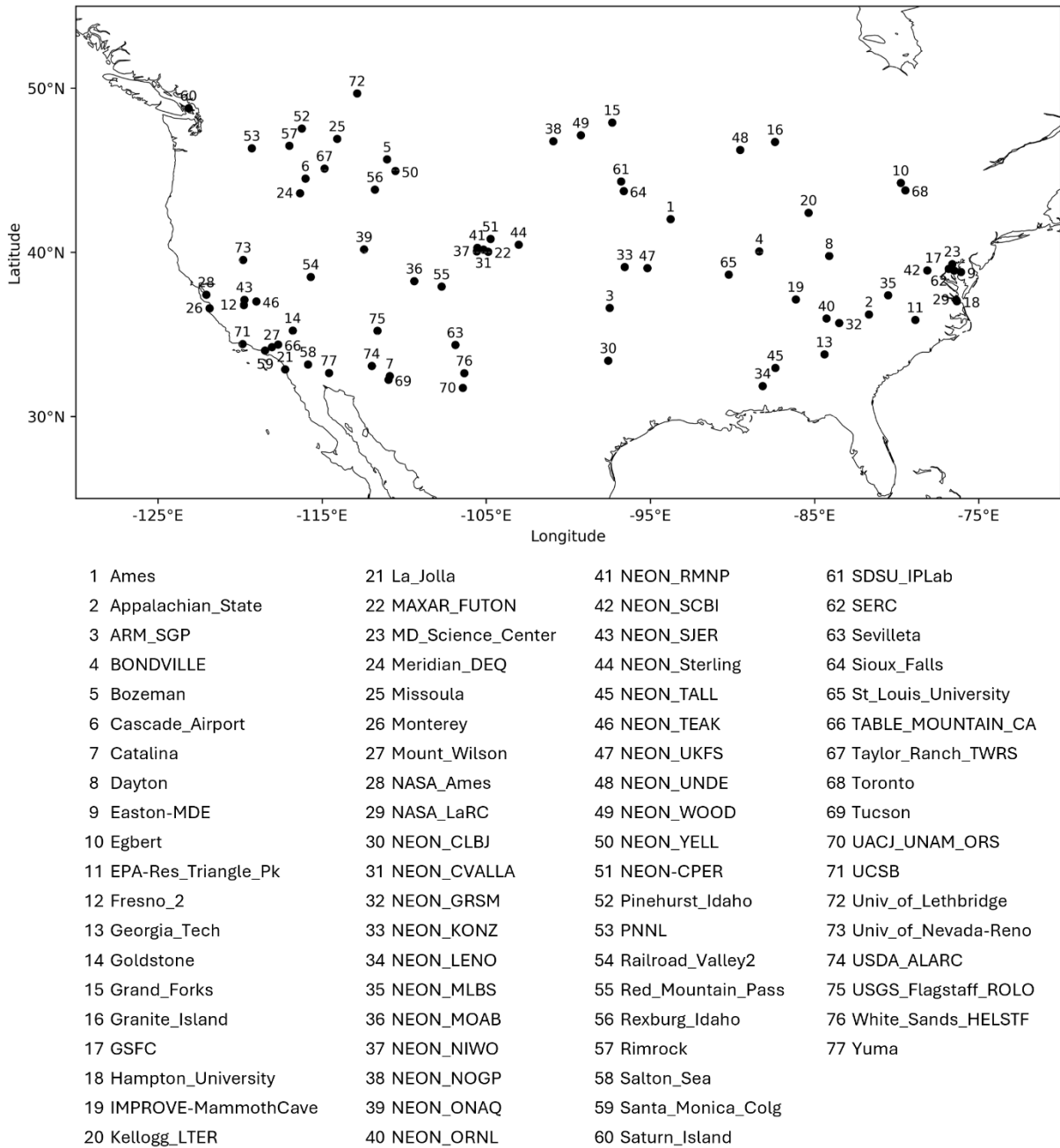


Figure A1: Locations of the 77 AERONET sites used in this study



675 Code and data availability

AERONET, accessed 2024: Aerosol Optical Depth, North America, September 2020 level 2 data.

Available online https://aeronet.gsfc.nasa.gov/new_web/draw_map_display_aod_v3.html?level=3

GFED4.1s, 2023: Daily Global Fire Emissions Database, Version 4.1 (beta), years 2019 and 2020.

Available online <https://www.geo.vu.nl/~gwerf/GFED/GFED4/>.

680 SNPP VIIRS: Suomi National Polar-orbiting Partnership, Visible Infrared Imaging Radiometer Suite, November 2019 –

December 2020, AERDB_D3_VIIRS_SNPP - VIIRS/SNPP Deep Blue Level 3 daily aerosol data, 1x1 degree grid

Available online

https://ladsweb.modaps.eosdis.nasa.gov/missions-and-measurements/products/AERDB_D3_VIIRS_SNPP

TROPOMI total column gridded CO data, 2020

685 The research data supporting this publication are openly available from the Zenodo repository:

Interactive computing environment- Representing extreme fires and their radiative effects in a global climate model via variable scaling of emissions: Case study of the 2020 California wildfires. Zenodo. <https://doi.org/10.5281/zenodo.16813001>

To run the scripts to produce the figures, first unzip the folders 'data' and 'snapshots'

Author contribution

690 EQ, BJ and JH designed the experiments. BJ performed the UKESM1.1 simulations. EQ carried out the observation–model comparisons and analysis. RV provided the gridded TROPOMI datasets. EQ prepared the manuscript with contributions from all co-authors.

Competing interests

The authors declare that they have no conflict of interest.

695 Acknowledgements

EQ and JH acknowledge funding under NERC TWISTA (The Wider-ranging Impacts of STRatospheric smoke Aerosol; NE/Y000021/1). JH, GvW, RV, SS, TE acknowledge support through ESA Contract No. 4000145351/24/I-LR.

We thank the Principal Investigators, Co-Is, and their staff (<https://aeronet.gsfc.nasa.gov>) for establishing and maintaining the 77 AERONET sites used in this investigation. We thank the Deep Blue science team (<https://deepblue.gsfc.nasa.gov>) for the VIIRS Deep Blue aerosol data record. We also acknowledge the use of imagery from the Worldview Snapshots application (<https://wvs.earthdata.nasa.gov>), part of the Earth Science Data and Information System (ESDIS).

700



For the purpose of open access, the author has applied a Creative Commons Attribution (CC BY) licence to any Author Accepted Manuscript version arising from this submission.

References

- 705 Andela, N., Morton, D. C., Giglio, L., Paugam, R., Chen, Y., Hantson, S., van der Werf, G. R., and Randerson, J. T.: The Global Fire Atlas of individual fire size, duration, speed and direction, *Earth Syst. Sci. Data*, 11, 529–552, <https://doi.org/10.5194/essd-11-529-2019>, 2019.
- Archibald, A. T., O'Connor, F. M., Abraham, N. L., Archer-Nicholls, S., Chipperfield, M. P., Dalvi, M., Folberth, G. A., Dennison, F., Dhomse, S. S., Griffiths, P. T., Hardacre, C., Hewitt, A. J., Hill, R., Johnson, C. E., Keeble, J., Köhler, M. O.,
710 Morgenstern, O., Mulchay, J. P., Ordóñez, C., Pope, R. J., Rumbold, S., Russo, M. R., Savage, N., Sellar, A., Stringer, M., Turnock, S., Wild, O., and Zeng, G.: Description and evaluation of the UKCA stratosphere-troposphere chemistry scheme (StratTrop vn 1.0) implemented in UKESM1, <https://doi.org/10.5194/gmd-2019-246>, 25 September 2019.
- Baars, H., Radenz, M., Floutsi, A. A., Engelmann, R., Althausen, D., Heese, B., Ansmann, A., Flament, T., Dabas, A., Traçon, D., Reitebuch, O., Bley, S., and Wandinger, U.: Californian Wildfire Smoke Over Europe: A First Example of the
715 Aerosol Observing Capabilities of Aeolus Compared to Ground-Based Lidar, *Geophysical Research Letters*, 48, e2020GL092194, <https://doi.org/10.1029/2020GL092194>, 2021.
- Boucher, O.: *Atmospheric Aerosols: Properties and Climate Impacts*, Springer Netherlands, Dordrecht, <https://doi.org/10.1007/978-94-017-9649-1>, 2015.
- Boucher, O., Randall, D., Artaxo, P., Bretherton, C., Feingold, G., Forster, P., Kerminen, V.-M., Kondo, Y., Liao, H.,
720 Lohmann, U., Rasch, P., Satheesh, S. K., Sherwood, S., Stevens, B., and Zhang, X. Y.: Clouds and Aerosols, in: *Climate Change 2013 – The Physical Science Basis*, edited by: IPCC, Cambridge University Press, 571–658, <https://doi.org/10.1017/CBO9781107415324.016>, 2014.
- Ceamanos, X., Coopman, Q., George, M., Riedi, J., Parrington, M., and Clerbaux, C.: Remote sensing and model analysis of biomass burning smoke transported across the Atlantic during the 2020 Western US wildfire season, *Sci Rep*, 13, 16014,
725 <https://doi.org/10.1038/s41598-023-39312-1>, 2023.
- Chen, H., Zhang, W., and Sheng, L.: Canadian record-breaking wildfires in 2023 and their impact on US air quality, *Atmospheric Environment*, Volume 342, 120941, ISSN 1352-2310, <https://doi.org/10.1016/j.atmosenv.2024.120941>, 2025.
- Chen, Y., Hall, J., van Wees, D., Andela, N., Hantson, S., Giglio, L., van der Werf, G. R., Morton, D. C., and Randerson, J. T.: Multi-decadal trends and variability in burned area from the fifth version of the Global Fire Emissions Database (GFED5), *Earth Syst. Sci. Data*, 15, 5227–5259, <https://doi.org/10.5194/essd-15-5227-2023>, 2023.
730
- Clark, D. B., Mercado, L. M., Sitch, S., Jones, C. D., Gedney, N., Best, M. J., Pryor, M., Rooney, G. G., Essery, R. L. H., Blyth, E., Boucher, O., Harding, R. J., Huntingford, C., and Cox, P. M.: The Joint UK Land Environment Simulator (JULES), model description – Part 2: Carbon fluxes and vegetation dynamics, *Geosci. Model Dev.*, 4, 701–722, <https://doi.org/10.5194/gmd-4-701-2011>, 2011.



- 735 de Graaf, M., Bellouin, N., Tilstra, L. G., Haywood, J., and Stammes, P.: Aerosol direct radiative effect of smoke over clouds over the southeast Atlantic Ocean from 2006 to 2009, *Geophysical Research Letters*, 41, 7723–7730, <https://doi.org/10.1002/2014GL061103>, 2014.
- Dee, D. P., Uppala, S. M., Simmons, A. J., Berrisford, P., Poli, P., Kobayashi, S., Andrae, U., Balmaseda, M. A., Balsamo, G., Bauer, P., Bechtold, P., Beljaars, A. C. M., van de Berg, L., Bidlot, J., Bormann, N., Delsol, C., Dragani, R., Fuentes, M.,
740 Geer, A. J., Haimberger, L., Healy, S. B., Hersbach, H., Hólm, E. V., Isaksen, L., Kållberg, P., Köhler, M., Matricardi, M., McNally, A. P., Monge-Sanz, B. M., Morcrette, J. -J., Park, B. -K., Peubey, C., de Rosnay, P., Tavolato, C., Thépaut, J. -N., and Vitart, F.: The ERA-Interim reanalysis: configuration and performance of the data assimilation system, *Quart J Royal Meteor Soc*, 137, 553–597, <https://doi.org/10.1002/qj.828>, 2011.
- Dennison, P. E., Brewer, S. C., Arnold, J. D., and Moritz, M. A.: Large wildfire trends in the western United States, 1984–
745 2011, *Geophysical Research Letters*, 41, 2928–2933, <https://doi.org/10.1002/2014GL059576>, 2014.
- Dentener, F., Kinne, S., Bond, T., Boucher, O., Cofala, J., Generoso, S., Ginoux, P., Gong, S., Hoelzemann, J. J., Ito, A., Marelli, L., Penner, J. E., Putaud, J.-P., Textor, C., Schulz, M., van der Werf, G. R., and Wilson, J.: Emissions of primary aerosol and precursor gases in the years 2000 and 1750 prescribed data-sets for AeroCom, *Atmos. Chem. Phys.*, 6, 4321–4344, <https://doi.org/10.5194/acp-6-4321-2006>, 2006.
- 750 Duane, A., Castellnou, M., and Brotons, L.: Towards a comprehensive look at global drivers of novel extreme wildfire events, *Climatic Change*, 165, 43, <https://doi.org/10.1007/s10584-021-03066-4>, 2021.
- Eck, T. F., Holben, B. N., Giles, D. M., Slutsker, I., Sinyuk, A., Schafer, J. S., Smirnov, A., Sorokin, M., Reid, J. S., Sayer, A. M., Hsu, N. C., Shi, Y. R., Levy, R. C., Lyapustin, A., Rahman, M. A., Liew, S., Salinas Cortijo, S. V., Li, T., Kalbermatter, D., Keong, K. L., Yuggotomo, M. E., Aditya, F., Mohamad, M., Mahmud, M., Chong, T. K., Lim, H., Choon,
755 Y. E., Deranadyan, G., Kusumaningtyas, S. D. A., and Aldrian, E.: AERONET Remotely Sensed Measurements and Retrievals of Biomass Burning Aerosol Optical Properties During the 2015 Indonesian Burning Season, *JGR Atmospheres*, 124, 4722–4740, <https://doi.org/10.1029/2018JD030182>, 2019.
- Eck, T. F., Holben, B. N., Reid, J. S., Sinyuk, A., Giles, D. M., Arola, A., Slutsker, I., Schafer, J. S., Sorokin, M. G., Smirnov, A., LaRosa, A. D., Kraft, J., Reid, E. A., O’Neill, N. T., Welton, E. J., and Menendez, A. R.: The extreme forest
760 fires in California/Oregon in 2020: Aerosol optical and physical properties and comparisons of aged versus fresh smoke, *Atmospheric Environment*, 305, 119798, <https://doi.org/10.1016/j.atmosenv.2023.119798>, 2023.
- Edwards, D. P., Emmons, L. K., Gille, J. C., Chu, A., Attié, J. -L., Giglio, L., Wood, S. W., Haywood, J., Deeter, M. N., Massie, S. T., Ziskin, D. C., and Drummond, J. R.: Satellite-observed pollution from Southern Hemisphere biomass burning, *J. Geophys. Res.*, 111, 2005JD006655, <https://doi.org/10.1029/2005JD006655>, 2006.
- 765 Ellis, T. M., Bowman, D. M. J. S., Jain, P., Flannigan, M. D., and Williamson, G. J.: Global increase in wildfire risk due to climate-driven declines in fuel moisture, *Global Change Biology*, 28, 1544–1559, <https://doi.org/10.1111/gcb.16006>, 2022.
- Forrister, H., Liu, J., Scheuer, E., Dibb, J., Ziemba, L., Thornhill, K. L., Anderson, B., Diskin, G., Perring, A. E., Schwarz, J. P., Campuzano-Jost, P., Day, D. A., Palm, B. B., Jimenez, J. L., Nenes, A., and Weber, R. J.: Evolution of brown carbon in wildfire plumes, *Geophysical Research Letters*, 42, 4623–4630, <https://doi.org/10.1002/2015GL063897>, 2015.



- 770 Forster, P., Storelvmo, T., Armour, K., Collins, W., Dufresne, J.-L., Frame, D., Lunt, D. J., Mauritsen, T., Palmer, M. D., Watanabe, M., Wild, M., and Zhang, H.: The Earth's Energy Budget, Climate Feedbacks, and Climate Sensitivity. In *Climate Change 2021: The Physical Science Basis. Contribution of Working Group I to the Sixth Assessment Report of the Intergovernmental Panel on Climate Change*, 1st ed., Cambridge University Press, <https://doi.org/10.1017/9781009157896.009>, 2021.
- 775 Giles, D. M., Sinyuk, A., Sorokin, M. G., Schafer, J. S., Smirnov, A., Slutsker, I., Eck, T. F., Holben, B. N., Lewis, J. R., Campbell, J. R., Welton, E. J., Korkin, S. V., and Lyapustin, A. I.: Advancements in the Aerosol Robotic Network (AERONET) Version 3 database – automated near-real-time quality control algorithm with improved cloud screening for Sun photometer aerosol optical depth (AOD) measurements, *Atmos. Meas. Tech.*, 12, 169–209, <https://doi.org/10.5194/amt-12-169-2019>, 2019.
- 780 Gumber, A., Reid, J. S., Holz, R. E., Eck, T. F., Hsu, N. C., Levy, R. C., Zhang, J., and Veglio, P.: Assessment of severe aerosol events from NASA MODIS and VIIRS aerosol products for data assimilation and climate continuity, *Atmos. Meas. Tech.*, 16, 2547–2573, <https://doi.org/10.5194/amt-16-2547-2023>, 2023.
- Haywood, J. M. and Shine, K. P.: The effect of anthropogenic sulfate and soot aerosol on the clear sky planetary radiation budget, *Geophysical Research Letters*, 22, 603–606, <https://doi.org/10.1029/95GL00075>, 1995.
- 785 Haywood, J. M., Abel, S. J., Barrett, P. A., Bellouin, N., Blyth, A., Bower, K. N., Brooks, M., Carslaw, K., Che, H., Coe, H., Cotterell, M. I., Crawford, I., Cui, Z., Davies, N., Dingley, B., Field, P., Formenti, P., Gordon, H., de Graaf, M., Herbert, R., Johnson, B., Jones, A. C., Langridge, J. M., Malavelle, F., Partridge, D. G., Peers, F., Redemann, J., Stier, P., Szpek, K., Taylor, J. W., Watson-Parris, D., Wood, R., Wu, H., and Zuidema, P.: The CLOUD–Aerosol–Radiation Interaction and Forcing: Year 2017 (CLARIFY-2017) measurement campaign, *Atmos. Chem. Phys.*, 21, 1049–1084, <https://doi.org/10.5194/acp-21-1049-2021>, 2021.
- 790 Hersbach, H., Bell, B., Berrisford, P., Hirahara, S., Horányi, A., Muñoz-Sabater, J., Nicolas, J., Peubey, C., Radu, R., Schepers, D., Simmons, A., Soci, C., Abdalla, S., Abellan, X., Balsamo, G., Bechtold, P., Biavati, G., Bidlot, J., Bonavita, M., de Chiara, G., Dahlgren, P., Dee, D., Diamantakis, M., Dragani, R., Flemming, J., Forbes, R., Fuentes, M., Geer, A., Haimberger, L., Healy, S., Hogan, R. J., Hólm, E., Janisková, M., Keeley, S., Laloyaux, P., Lopez, P., Lupu, C., Radnoti, G., de Rosnay, P., Rozum, I., Vamborg, F., Villaume, S., and Thépaut, J.: The ERA5 global reanalysis, *Quart J Royal Meteor Soc*, 146, 1999–2049, <https://doi.org/10.1002/qj.3803>, 2020.
- 795 Holben, B. N., Eck, T. F., Slutsker, I., Tanré, D., Buis, J. P., Setzer, A., Vermote, E., Reagan, J. A., Kaufman, Y. J., Nakajima, T., Lavenue, F., Jankowiak, I., and Smirnov, A.: AERONET—A Federated Instrument Network and Data Archive for Aerosol Characterization, Remote Sensing of Environment, 66, 1–16, [https://doi.org/10.1016/S0034-4257\(98\)00031-5](https://doi.org/10.1016/S0034-4257(98)00031-5), 1998.
- 800 Jackson, J. M., Liu, H., Laszlo, I., Kondragunta, S., Remer, L. A., Huang, J., and Huang, H.: Suomi-NPP VIIRS aerosol algorithms and data products, *JGR Atmospheres*, 118, <https://doi.org/10.1002/2013JD020449>, 2013.
- Jin, Y., and Roy, D. P.: Fire-induced albedo change and its radiative forcing at the surface in northern Australia, *Geophys. Res. Lett.*, 32, L13401, <https://doi.org/10.1029/2005GL022822>, 2005.



- 805 Johnson, B. T. and Haywood, J. M.: Assessing the Impact of Self-Lofting on Increasing the Altitude of Black Carbon in a Global Climate Model, *JGR Atmospheres*, 128, <https://doi.org/10.1029/2022JD038039>, 2023.
- Johnson, B. T., Haywood, J. M., Langridge, J. M., Darbyshire, E., Morgan, W. T., Szpek, K., Brooke, J. K., Marengo, F., Coe, H., Artaxo, P., Longo, K. M., Mulcahy, J. P., Mann, G. W., Dalvi, M., and Bellouin, N.: Evaluation of biomass burning aerosols in the HadGEM3 climate model with observations from the SAMBBA field campaign, *Atmos. Chem. Phys.*, 16, 14657–14685, <https://doi.org/10.5194/acp-16-14657-2016>, 2016.
- 810 Johnson, B. T., Haywood, J. M., and Hawcroft, M. K.: Are Changes in Atmospheric Circulation Important for Black Carbon Aerosol Impacts on Clouds, Precipitation, and Radiation?, *JGR Atmospheres*, 124, 7930–7950, <https://doi.org/10.1029/2019JD030568>, 2019.
- Johnston, F. H., Henderson, S. B., Chen, Y., Randerson, J. T., Marlier, M., DeFries, R. S., Kinney, P., Bowman, D. M. J. S., and Brauer, M.: Estimated Global Mortality Attributable to Smoke from Landscape Fires, *Environ Health Perspect*, 120, 695–701, <https://doi.org/10.1289/ehp.1104422>, 2012.
- 815 Jones, M. W., Abatzoglou, J. T., Veraverbeke, S., Andela, N., Lasslop, G., Forkel, M., et al.: Global and regional trends and drivers of fire under climate change. *Reviews of Geophysics*, 60, e2020RG000726. <https://doi.org/10.1029/2020RG000726>, 2022.
- 820 Jones, M. W., Veraverbeke, S., Andela, N., Doerr, S. H., Kolden, C., Mataveli, G., Pettinari, M. L., Le Quéré, C., Rosan, T. M., van der Werf, G. R., van Wees, D., and Abatzoglou, J. T.: Global rise in forest fire emissions linked to climate change in the extratropics, *Science*, 386, <https://doi.org/10.1126/science.adl5889>, 2024.
- Khalil, M.A.K., and Rasmussen, R.A.: The global cycle of carbon monoxide: Trends and mass balance, *Chemosphere*, Volume 20, Issues 1–2, Pages 227–242, ISSN 0045-6535, [https://doi.org/10.1016/0045-6535\(90\)90098-E](https://doi.org/10.1016/0045-6535(90)90098-E), 1990.
- 825 Kuhlbrodt, T., Jones, C. G., Sellar, A., Storkey, D., Blockley, E., Stringer, M., Hill, R., Graham, T., Ridley, J., Blaker, A., Calvert, D., Copsey, D., Ellis, R., Hewitt, H., Hyder, P., Ineson, S., Mulcahy, J., Siahayan, A., and Walton, J.: The Low-Resolution Version of HadGEM3 GC3.1: Development and Evaluation for Global Climate, *J Adv Model Earth Syst*, 10, 2865–2888, <https://doi.org/10.1029/2018MS001370>, 2018.
- 830 Li, J., Carlson, B. E., Yung, Y. L., Lv, D., Hansen, J., Penner, J. E., Liao, H., Ramaswamy, V., Kahn, R. A., Zhang, P., Dubovik, O., Ding, A., Lacis, A. A., Zhang, L., and Dong, Y.: Scattering and absorbing aerosols in the climate system, *Nat Rev Earth Environ*, 3, 363–379, <https://doi.org/10.1038/s43017-022-00296-7>, 2022.
- Li, Y., Tong, D., Jeon, Y., Lee, B. S., Park, J., Kondragunta, S., Zhang, X., Siripun, N., Song, S., Mehta, C., and Chen, J. Z.: Using AOD and UVAI to Reduce the Uncertainties in Wildfire Emission and Air Quality Modeling, *JGR Atmospheres*, 130, <https://doi.org/10.1029/2024jd041816>, 2025.
- 835 Lin, L. I.-K.: A Concordance Correlation Coefficient to Evaluate Reproducibility, *Biometrics*, 45, 255, <https://doi.org/10.2307/2532051>, 1989.
- Linley, G. D., Jolly, C. J., Doherty, T. S., Geary, W. L., Armenteras, D., Belcher, C. M., Bliege Bird, R., Duane, A., Fletcher, M., Giorgis, M. A., Haslem, A., Jones, G. M., Kelly, L. T., Lee, C. K. F., Nolan, R. H., Parr, C. L., Pausas, J. G.,



- Price, J. N., Regos, A., Ritchie, E. G., Ruffault, J., Williamson, G. J., Wu, Q., and Nimmo, D. G.: What do you mean, 'megafire'?, *Global Ecol Biogeogr*, 31, 1906–1922, <https://doi.org/10.1111/geb.13499>, 2022.
- Mann, G. W., Carslaw, K. S., Spracklen, D. V., Ridley, D. A., Manktelow, P. T., Chipperfield, M. P., Pickering, S. J., and Johnson, C. E.: Description and evaluation of GLOMAP-mode: a modal global aerosol microphysics model for the UKCA composition-climate model, *Geosci. Model Dev.*, 3, 519–551, <https://doi.org/10.5194/gmd-3-519-2010>, 2010.
- Marlier, M. E., DeFries, R. S., Voulgarakis, A., Kinney, P. L., Randerson, J. T., Shindell, D. T., Chen, Y., and Faluvegi, G.: El Niño and health risks from landscape fire emissions in southeast Asia, *Nature Clim Change*, 3, 131–136, <https://doi.org/10.1038/nclimate1658>, 2013.
- Matichuk, R. I., Colarco, P. R., Smith, J. A., and Toon, O. B.: Modeling the transport and optical properties of smoke plumes from South American biomass burning, *J. Geophys. Res.*, 113, 2007JD009005, <https://doi.org/10.1029/2007JD009005>, 2008.
- Mulcahy, J. P., Jones, C., Sellar, A., Johnson, B., Boutle, I. A., Jones, A., Andrews, T., Rumbold, S. T., Mollard, J., Bellouin, N., Johnson, C. E., Williams, K. D., Grosvenor, D. P., and McCoy, D. T.: Improved Aerosol Processes and Effective Radiative Forcing in HadGEM3 and UKESM1, *J Adv Model Earth Syst*, 10, 2786–2805, <https://doi.org/10.1029/2018MS001464>, 2018.
- Mulcahy, J. P., Johnson, C., Jones, C. G., Povey, A. C., Scott, C. E., Sellar, A., Turnock, S. T., Woodhouse, M. T., Abraham, N. L., Andrews, M. B., Bellouin, N., Browse, J., Carslaw, K. S., Dalvi, M., Folberth, G. A., Glover, M., Grosvenor, D. P., Hardacre, C., Hill, R., Johnson, B., Jones, A., Kipling, Z., Mann, G., Mollard, J., O'Connor, F. M., Palmiéri, J., Reddington, C., Rumbold, S. T., Richardson, M., Schutgens, N. A. J., Stier, P., Stringer, M., Tang, Y., Walton, J., Woodward, S., and Yool, A.: Description and evaluation of aerosol in UKESM1 and HadGEM3-GC3.1 CMIP6 historical simulations, *Geosci. Model Dev.*, 13, 6383–6423, <https://doi.org/10.5194/gmd-13-6383-2020>, 2020.
- Mulcahy, J. P., Jones, C. G., Rumbold, S. T., Kuhlbrodt, T., Dittus, A. J., Blockley, E. W., Yool, A., Walton, J., Hardacre, C., Andrews, T., Bodas-Salcedo, A., Stringer, M., de Mora, L., Harris, P., Hill, R., Kelley, D., Robertson, E., and Tang, Y.: UKESM1.1: development and evaluation of an updated configuration of the UK Earth System Model, *Geosci. Model Dev.*, 16, 1569–1600, <https://doi.org/10.5194/gmd-16-1569-2023>, 2023.
- Nolan, R. H., Anderson, L. O., Poulter, B., and Varner, J. M.: Increasing threat of wildfires: the year 2020 in perspective: A Global Ecology and Biogeography special issue, *Global Ecol Biogeogr*, 31, 1898–1905, <https://doi.org/10.1111/geb.13588>, 2022.
- Peers, F. P.N. Francis, S.J. Abel, P.A. Barrett, K.N. Bower, M.I. Cotterell, I. Crawford, N.W. Davies, C. Fox, S. Fox, J.M. Langridge, K.G. Meyer, S.E. Platnick, K. Szpek and J.M. Haywood, Observation of absorbing aerosols above clouds over the South-East Atlantic Ocean from the geostationary satellite SEVIRI - Part 2: Comparison with MODIS and aircraft measurements from the CLARIFY-2017 field campaign, *Atmos. Chem. Phys.*, 21, 3235–3254, <https://doi.org/10.5194/acp-21-3235-2021>
- Petrenko, M., Kahn, R., Chin, M., Bauer, S. E., Bergman, T., Bian, H., Curci, G., Johnson, B., Kaiser, J. W., Kipling, Z., Kokkola, H., Liu, X., Mezuman, K., Mielonen, T., Myhre, G., Pan, X., Protonotariou, A., Remy, S., Skeie, R. B., Stier, P., Takemura, T., Tsigaridis, K., Wang, H., Watson-Parris, D., and Zhang, K.: Biomass burning emission analysis based on



- 875 MODIS aerosol optical depth and AeroCom multi-model simulations: implications for model constraints and emission inventories, *Atmos. Chem. Phys.*, 25, 1545–1567, <https://doi.org/10.5194/acp-25-1545-2025>, 2025.
- Potter, C. S., Randerson, J. T., Field, C. B., Matson, P. A., Vitousek, P. M., Mooney, H. A., and Klooster, S. A.: Terrestrial ecosystem production: A process model based on global satellite and surface data, *Global Biogeochemical Cycles*, 7, 811–841, <https://doi.org/10.1029/93GB02725>, 1993.
- 880 Ramo, R., Ekhi R., Bistinas, I., van Wees, D., Bastarrika, A., Chuvieco, E., and van der Werf, Guido.: African burned area and fire carbon emissions are strongly impacted by small fires undetected by coarse resolution satellite data. *Proceedings of the National Academy of Sciences*. 118. e2011160118. [10.1073/pnas.2011160118](https://doi.org/10.1073/pnas.2011160118), 2021.
- Randerson, J. T., Liu, H., Flanner, M. G., Chambers, S. D., Jin, Y., Hess, P. G., Pfister, G., Mack, M. C., Treseder, K. K., Welp, L. R., Chapin, F. S., Harden, J. W., Goulden, M. L., Lyons, E., Neff, J. C., Schuur, E. A. G., and Zender, C. S.: The
885 Impact of Boreal Forest Fire on Climate Warming, *Science*, 314, 1130–1132, <https://doi.org/10.1126/science.1132075>, 2006.
- Randerson, J. T., Y. Chen, G. R. van der Werf, B. M. Rogers, and D. C. Morton.: Global burned area and biomass burning emissions from small fires, *J. Geophys. Res.*, 117, G04012, [doi:10.1029/2012JG002128](https://doi.org/10.1029/2012JG002128), 2012.
- Randerson, J. T., van der Werf, G. R., Giglio, L., Collatz, G. J., and Kasibhatla, P. S.: Global Fire Emissions Database, Version 4.1 (GFEDv4), 1925.7122549999906 MB, <https://doi.org/10.3334/ORNLDAC/1293>, 2017.
- 890 Reddington, C. L., Spracklen, D. V., Artaxo, P., Ridley, D. A., Rizzo, L. V., and Arana, A.: Analysis of particulate emissions from tropical biomass burning using a global aerosol model and long-term surface observations, *Atmos. Chem. Phys.*, 16, 11083–11106, <https://doi.org/10.5194/acp-16-11083-2016>, 2016.
- Robock, A.: Enhancement of Surface Cooling Due to Forest Fire Smoke, *Science*, 242, 911–913, <https://doi.org/10.1126/science.242.4880.911>, 1988.
- 895 Sakaeda, N., Wood, R., and Rasch, P. J.: Direct and semidirect aerosol effects of southern African biomass burning aerosol, *J. Geophys. Res.*, 116, D12205, <https://doi.org/10.1029/2010JD015540>, 2011.
- Sawyer, V., Levy, R. C., Mattoo, S., Cureton, G., Shi, Y., and Remer, L. A.: Continuing the MODIS Dark Target Aerosol Time Series with VIIRS, *Remote Sensing*, 12, 308, <https://doi.org/10.3390/rs12020308>, 2020.
- Schuster, G. L., Dubovik, O., and Holben, B. N.: Angstrom exponent and bimodal aerosol size distributions, *J. Geophys. Res.*, 111, 2005JD006328, <https://doi.org/10.1029/2005JD006328>, 2006.
900
- Sellar, A. A., Jones, C. G., Mulcahy, J. P., Tang, Y., Yool, A., Wiltshire, A., O'Connor, F. M., Stringer, M., Hill, R., Palmieri, J., Woodward, S., de Mora, L., Kuhlbrodt, T., Rumbold, S. T., Kelley, D. I., Ellis, R., Johnson, C. E., Walton, J., Abraham, N. L., Andrews, M. B., Andrews, T., Archibald, A. T., Berthou, S., Burke, E., Blockley, E., Carslaw, K., Dalvi, M., Edwards, J., Folberth, G. A., Gedney, N., Griffiths, P. T., Harper, A. B., Hendry, M. A., Hewitt, A. J., Johnson, B.,
905 Jones, A., Jones, C. D., Keeble, J., Liddicoat, S., Morgenstern, O., Parker, R. J., Predoi, V., Robertson, E., Siahann, A., Smith, R. S., Swaminathan, R., Woodhouse, M. T., Zeng, G., and Zerroukat, M.: UKESM1: Description and Evaluation of the U.K. Earth System Model, *J Adv Model Earth Syst*, 11, 4513–4558, <https://doi.org/10.1029/2019MS001739>, 2019.



- Sellar, A. A., Walton, J., Jones, C. G., Wood, R., Abraham, N. L., Andrejczuk, M., Andrews, M. B., Andrews, T., Archibald, A. T., de Mora, L., Dyson, H., Elkington, M., Ellis, R., Florek, P., Good, P., Gohar, L., Haddad, S., Hardiman, S. C., Hogan, E., Iwi, A., Jones, C. D., Johnson, B., Kelley, D. I., Kettleborough, J., Knight, J. R., Köhler, M. O., Kuhlbrodt, T., Liddicoat, S., Linova-Pavlova, I., Mizielinski, M. S., Morgenstern, O., Mulcahy, J., Neininger, E., O'Connor, F. M., Petrie, R., Ridley, J., Rioual, J., Roberts, M., Robertson, E., Rumbold, S., Seddon, J., Shepherd, H., Shim, S., Stephens, A., Teixeira, J. C., Tang, Y., Williams, J., Wiltshire, A., and Griffiths, P. T.: Implementation of U.K. Earth System Models for CMIP6, *J Adv Model Earth Syst*, 12, e2019MS001946, <https://doi.org/10.1029/2019MS001946>, 2020.
- 915 Shinozuka, Y., Saide, P. E., Ferrada, G. A., Burton, S. P., Ferrare, R., Doherty, S. J., Gordon, H., Longo, K., Mallet, M., Feng, Y., Wang, Q., Cheng, Y., Dobracki, A., Freitag, S., Howell, S. G., LeBlanc, S., Flynn, C., Segal-Rosenhaimer, M., Pistone, K., Podolske, J. R., Stith, E. J., Bennett, J. R., Carmichael, G. R., Da Silva, A., Govindaraju, R., Leung, R., Zhang, Y., Pfister, L., Ryoo, J.-M., Redemann, J., Wood, R., and Zuidema, P.: Modeling the smoky troposphere of the southeast Atlantic: a comparison to ORACLES airborne observations from September of 2016, *Atmos. Chem. Phys.*, 20, 11491–
- 920 11526, <https://doi.org/10.5194/acp-20-11491-2020>, 2020.
- Smirnov, A., Holben, B. N., Eck, T. F., Dubovik, O., and Slutsker, I.: Cloud-Screening and Quality Control Algorithms for the AERONET Database, *Remote Sensing of Environment*, 73, 337–349, [https://doi.org/10.1016/S0034-4257\(00\)00109-7](https://doi.org/10.1016/S0034-4257(00)00109-7), 2000.
- Smith, A. B.: U.S. Billion-dollar Weather and Climate Disasters, 1980 - present (NCEI Accession 0209268),
- 925 <https://doi.org/10.25921/STKW-7W73>, 2020.
- Thornhill, G. D., Ryder, C. L., Highwood, E. J., Shaffrey, L. C., and Johnson, B. T.: The effect of South American biomass burning aerosol emissions on the regional climate, *Atmos. Chem. Phys.*, 18, 5321–5342, <https://doi.org/10.5194/acp-18-5321-2018>, 2018.
- United Nations Environment Programme: Spreading like Wildfire – The Rising Threat of Extraordinary Landscape Fires,
- 930 2022.
- van der Velde, I. R., van der Werf, G. R., van Wees, D., Schutgens, N. A. J., Vernooij, R., Houweling, S., et al. (2024). Small fires, big impact: Evaluating fire emission estimates in southern Africa using new satellite imagery of burned area and carbon monoxide. *Geophysical Research Letters*, 51, e2023GL106122. <https://doi.org/10.1029/2023GL106122>
- van der Werf, G. R., Randerson, J. T., Giglio, L., van Leeuwen, T. T., Chen, Y., Rogers, B. M., Mu, M., van Marle, M. J. E.,
- 935 Morton, D. C., Collatz, G. J., Yokelson, R. J., and Kasibhatla, P. S.: Global fire emissions estimates during 1997–2016, *Earth Syst. Sci. Data*, 9, 697–720, <https://doi.org/10.5194/essd-9-697-2017>, 2017.
- van Marle, M. J. E., Kloster, S., Magi, B. I., Marlon, J. R., Danianu, A.-L., Field, R. D., Arneth, A., Forrest, M., Hantson, S., Kehrwald, N. M., Knorr, W., Lasslop, G., Li, F., Mangeon, S., Yue, C., Kaiser, J. W., and van der Werf, G. R.: Historic global biomass burning emissions for CMIP6 (BB4CMIP) based on merging satellite observations with proxies and fire
- 940 models (1750–2015), *Geosci. Model Dev.*, 10, 3329–3357, <https://doi.org/10.5194/gmd-10-3329-2017>, 2017.
- Veefkind, J. P., Aben, I., McMullan, K., Förster, H., de Vries, J., Otter, G., Claas, J., Eskes, H. J., de Haan, J. F., Kleipool, Q., van Weele, M., Hasekamp, O., Hoozeveld, R., Landgraf, J., Snel, R., Tol, P., Ingmann, P., Voors, R., Kruizinga, B., Vink, R., Visser, H., and Levelt, P. F.: TROPOMI on the ESA Sentinel-5 Precursor: A GMES mission for global



- observations of the atmospheric composition for climate, air quality and ozone layer applications, *Remote Sensing of Environment*, 120, 70–83, <https://doi.org/10.1016/j.rse.2011.09.027>, 2012.
- Vernooij, R., Eames, T., Russell-Smith, J., Yates, C., Beatty, R., Evans, J., Edwards, A., Ribeiro, N., Wooster, M., Strydom, T., Giongo, M. V., Borges, M. A., Menezes Costa, M., Barradas, A. C. S., van Wees, D., and Van der Werf, G. R.: Dynamic savanna burning emission factors based on satellite data using a machine learning approach, *Earth Syst. Dynam.*, 14, 1039–1064, <https://doi.org/10.5194/esd-14-1039-2023>, 2023.
- 950 Wang, Q., Li, S., Yang, J., and Zhou, D.: Evaluation and comparison of VIIRS dark target and deep blue aerosol products over land, *Science of The Total Environment*, 869, 161667, <https://doi.org/10.1016/j.scitotenv.2023.161667>, 2023.
- Ward, D. S., Kloster, S., Mahowald, N. M., Rogers, B. M., Randerson, J. T., and Hess, P. G.: The changing radiative forcing of fires: global model estimates for past, present and future, *Atmos. Chem. Phys.*, 12, 10857–10886, <https://doi.org/10.5194/acp-12-10857-2012>, 2012.
- 955 Woodward, S.: Modeling the atmospheric life cycle and radiative impact of mineral dust in the Hadley Centre climate model, *J. Geophys. Res.*, 106, 18155–18166, <https://doi.org/10.1029/2000JD900795>, 2001.
- Yool, A., Popova, E. E., and Anderson, T. R.: MEDUSA-2.0: an intermediate complexity biogeochemical model of the marine carbon cycle for climate change and ocean acidification studies, *Geosci. Model Dev.*, 6, 1767–1811, <https://doi.org/10.5194/gmd-6-1767-2013>, 2013.
- 960 Zhao, J., Ciais, P., Chevallier, F., Canadell, J. G., van der Velde, I. R., Chuvieco, E., Chen, Y., Zhang, Q., He, K., and Zheng, B.: Enhanced CH₄ emissions from global wildfires likely due to undetected small fires, *Nat Commun*, 16, 804, <https://doi.org/10.1038/s41467-025-56218-w>, 2025.
- Zheng, B., Chevallier, F., Yin, Y., Ciais, P., Fortems-Cheiney, A., Deeter, M. N., Parker, R. J., Wang, Y., Worden, H. M., and Zhao, Y.: Global atmospheric carbon monoxide budget 2000–2017 inferred from multi-species atmospheric inversions, *Earth Syst. Sci. Data Discuss.*, 1, 1–42, <https://doi.org/10.5194/essd-2019-61>, 2019.
- 965